Effects of fluctuating magnetic field on the growth of the Kelvin-Helmholtz instability at the Earth's magnetopause

T. K. M. Nakamura[1], J. E. Stawarz[2], H. Hasegawa[3], Y. Narita[1], L. Franci[4], H. D. Wilder[5], R. Nakamura[1], and W. D. Nystrom[6]

[1] Space Research Institute, Austrian Academy of Sciences, Graz 8010, Austria.

[2] Department of Physics, Imperial College London, London, UK.

[3] Institute of Space and Astronautical Science, Japan Aerospace Exploration Agency, Sagamihara, Japan.

[4] School of Physics and Astronomy, Queen Mary University of London, London, UK.

[5] Laboratory for Atmospheric and Space Physics, University of Colorado Boulder, Boulder, Colorado, USA.

[6] Los Alamos National Laboratory, Los Alamos, New Mexico 87545, USA.

Corresponding author: Takuma Nakamura (takuma.tkm.nakamura@gmail.com)

Key Points:

- 2-D fully kinetic simulations of magnetopause Kelvin-Helmholtz instability initially imposing power-law field fluctuations are performed.
- The growth of the instability especially for long wavelength modes is enhanced by the fluctuating field, leading to more efficient mixing.
- Spectral features obtained from the simulations are in reasonable agreement with past spacecraft observations at the Earth's magnetopause.

Abstract

At the Earth's magnetopause, the Kelvin-Helmholtz (KH) instability, driven by the persistent velocity shear between the magnetosheath and the magnetosphere, has been frequently observed during northward interplanetary magnetic field (IMF) periods and considered as one of the most important candidates for transporting and mixing plasmas across the magnetopause. However, how this process interacts with magnetic field fluctuations, which persistently exist near the magnetopause, has been less discussed. Here we perform a series of 2-D fully kinetic simulations of the KH instability at the magnetopause considering a power-law spectrum of initial fluctuations in the magnetic field. The simulations demonstrate that when the amplitude level of the initial fluctuations is sufficiently large, the KH instability evolves faster, leading to a more efficient plasma mixing within the vortex layer. In addition, when the spectral index of the initial fluctuations is sufficiently small, the modes whose wavelength is longer than the theoretical fastest growing mode grow dominantly. The fluctuating magnetic field also results in the formation of the well-matured turbulent spectrum with a -5/3 index within the vortex layer even in the early non-linear growth phase of the KH instability. The obtained spectral features in the simulations are in reasonable agreement with the features in KH waves events at the magnetopause observed by the Magntospheric Multiscale (MMS) mission and conjunctively by the Geotail and Cluster spacecraft. These results indicate that the magnetic field fluctuations may really contribute to enhancing the wave activities especially for longer wavelength modes and the associated mixing at the magnetopause.

1. Introduction

The Kelvin-Helmholtz (KH) instability has long been considered as an important process for inducing efficient mass, momentum and energy transfer across sheared boundary layers in collisionless plasmas. At the Earth's magnetopause, for example, the KH instability is driven by the persistent velocity shear between the magnetosheath (shocked solar wind) and the magnetosphere [e.g., Dungey 1955], and is believed to effectively contribute to forming the Earth's low-latitude boundary layer (LLBL) where plasmas from magnetosheath and magnetospheric origins are mixed [e.g., Nakamura et al., 2019 and references therein]. Indeed, past in-situ spacecraft observations have revealed that surface waves and non-linear flow vortices, which could be generated by the KH instability, are frequently observed along the low-latitude magnetopause under steady and strong northward interplanetary magnetic field (IMF) [e.g., Sckopke et al., 1981; Kokubun et al., 1994; Slinker et al., 2003; Kivelson & Chen, 1995; Fairfield et al., 2000; Hasegawa et al., 2004, 2006; Foullon et al., 2008; Kavosi & Raeder, 2015; Moore et al., 2016].

When the IMF is strongly northward, although the magnetic shear is too small across the magnetopause and the shear layer is too thick to cause a rapid growth of spontaneous magnetic reconnection, the flow of the KH vortex can locally compress the thick layer and induce fast reconnection [Nakamura et al., 2006, 2008]. A series of recent 2-D and 3-D fully kinetic simulations have suggested that this so-called vortex-induced reconnection (VIR) process leads to efficient plasma mixing within the vortex through the formation of multiple magnetic islands (flux ropes) along the compressed layer [Nakamura et al., 2011, 2013; Daughton et al., 2014]. This vortex-induced flux rope formation has indeed been observed by the Time History of Events and Macroscale Interaction during Substorms (THEMIS) spacecraft at the dusk-flank magnetopause [Nakamura et al., 2013].

More recently, based on full high-time-resolution fields and plasma data by the Magnetospheric Multiscale (MMS) mission [Burch et al., 2016], electron and ion-scale VIR signatures were directly observed for the first time at the postnoon magnetopause on 8 September 2015 [Eriksson et al., 2016a,b; Li et al., 2016; Vernisse et al., 2016]. Nakamura et al. [2017a,b] successfully reproduced the observed VIR signatures in a 3-D fully kinetic simulation of this MMS event. In the simulation, the VIR is first induced in the early non-linear growth

phase of the KH instability and the local VIR signatures in this phase, such as the structures of the electron-scale central reconnection region called the electron diffusion region, the ion-scale outflow jets and the Hall magnetic field, are quantitatively consistent with the observed signatures [Nakamura et al., 2017,a,b; Sturner et al., 2018]. These consistencies indicate that the observed KH waves at the MMS location (~16 magnetic local time, MLT) were in an early non-linear growth phase. Based on the consistencies, the simulation predicted that the VIR and the subsequent turbulent formation of the flux ropes cause an efficient plasma mixing in later non-linear phases and globally forms a thick flank-to-tail LLBL during this event.

The simulation of the above MMS event further demonstrated that as the VIR develops, the spectral powers of the magnetic field and plasma flow fluctuations are significantly enhanced across sub-ion and magnetohydrodynamic (MHD) scales [Nakamura et al., 2017a]. The spectral index of the magnetic field fluctuations in the simulation in the early non-linear phase, in which the simulation agree well with the MMS observations on the local VIR signatures, is close to -8/3 at MHD scales (i.e., larger than ion scales), while the more well-matured Kolomogorov-like turbulent spectra with an index close to -5/3 appear in the later phases (see Figure 2 in Nakamura et al. [2017a]). However, using high-time-resolution MMS data, Stawarz et al. [2016] examined turbulent fluctuations in this MMS event and showed well-matured turbulent spectra with an index close to -5/3 at MHD scales. This indicates that there may be additional sources that drive the turbulence even before the early non-linear growth phase of the KH instability during this MMS event.

In this paper, based on 2-D fully kinetic simulations of this MMS event, we examine effects of initially-fluctuating magnetic field on the growth of the KH instability and the associated turbulence evolution within the vortex layer. Although the strong magnetic field fluctuations have frequently been observed in the magnetosheath [e.g., Luhmann et al., 1986; Alexandrova et al., 2008; Roberts et al., 2018], past simulation studies of the KH instability at the magnetopause have not considered these pre-existing fluctuations – i.e., setting up only laminar conditions. Here we newly setup initial magnetic field fluctuations with turbulent spectra. The new simulations demonstrate that the initial fluctuations enhance the growth of the KH instability over a broad range of scales, which leads to the formation of well-matured spectra with a -5/3 index even in the early non-linear phase. The results reasonably agree with the observations of this MMS event as well as an earlier event in which Geotail and Cluster

simultaneously observed different amplitudes of the KH waves at different locations of the magnetopause [Hasegawa et al., 2009].

This paper is organized as follows. Section 2 describes the details of the simulation model employed in this paper. Section 3 presents the obtained simulation results, while in Section 4 we summarize the results and discuss the realistic role of the pre-existing magnetic field fluctuations on the KH instability through the comparison of the simulation results with past in-situ observations of the KH waves at the magnetopause.

2. Model

2.1 Simulation settings

We perform a series of 2-D simulations of the KH instability induced at the magnetopause, using the fully kinetic particle-in-cell code VPIC [Bowers et al., 2008, 2009]. The initial simulation settings are the same as the ones employed in Nakamura et al. [2017a,b] except for the in-plane magnetic field components, the tilt angle of the shearing flow from the direction of the k-vector of the KH instability and the associated ion pressure balance across the velocity shear boundary. In Nakamura et al. [2017a,b], the initial density, magnetic field and ion bulk velocities across the magnetopause boundary layer were set to the values obtained from the MMS observations before and after the KH wave interval 10:20-11:26 UT on 8 September 2015 [Eriksson et al., 2016]; denoting the high-density magnetosheath and low-density magnetospheric (boundary layer) sides as 1 and 2, respectively, the shearing flow $\mathbf{U}_1$-$\mathbf{U}_2$=(U_{x1}, U_{y1}, U_{z1})=($V_0\cos\theta$, 0, $V_0\sin\theta$) along the magnetopause was slightly tilted θ=8.3° from the x-direction, and the magnetic field varied from (B_{x1}, B_{y1}, B_{z1})=(-0.1B_0, 0, B_0) to (B_{x1}, B_{y1}, B_{z1})=(0.2B_0, 0, B_0) across the boundary, where B_0 is the strength of the uniform guide field. Here, *x*-direction is along the **k**-vector of the fastest growing KH mode, *y*-direction is normal outward to the magnetopause, and $\mathbf{z}=\mathbf{x}\times\mathbf{y}$ completes the system. In this paper, to fit the 2-D study, the flow tilt angle and the in-plane field variation are slightly modified to θ=0° and (B_{x1}, B_{x2})=(-0.15B_0, 0.15B_0), respectively. The density ratio is set to be n_2/n_1=0.3, and the normalized parameters are set to be $n_1=n_0$=25cm^{-3}, B_0=74nT, $|V_0|$=355km/s=1.1V_A based on n_0 and B_0, as employed in Nakamura et al. [2017a,b]. The initial density, field and flow components are set by

connecting the above values using a tanh(y/D_0) function [Nakamura & Daughton, 2014], where D_0=3.33d_i is the initial half thickness of the shear layer and d_i=c/ω_{pi} is the ion inertial length based on n_0. To set the bulk velocities, particles are initialized with drifting Maxwellian velocities. The electron temperature is set as uniform, while the ion temperature is set to satisfy pressure balance, where the ion-to-electron temperature ratio in the magnetosheath is set to T_{i1}/T_{e0}=3.0. Additional electron and ion flows are set to satisfy the Harris type variation of B_x. The electric field is set to satisfy $\mathbf{E}=-\mathbf{U}_e\times\mathbf{B}$ and the electron density near the current sheet is set to be slightly higher than the ion density in the shear layer to satisfy the Gauss law [Pritchett and Coroniti, 1984]. The ion-to-electron mass ratio is m_i/m_e=25 unless otherwise noted, and the ratio between the electron plasma frequency and the gyrofrequency based on n_0 and B_0 is ω_{pe}/Ω_e = 1.0. The system size is set to be $L_x\times L_y$=200$d_i\times$300d_i=4096$\times$6144 cells with a total of 2.5×10^{10} superparticles. The system is periodic in *x*, and *y* boundaries are modeled as perfect conductors for the fields and reflecting for the particles.

2.2 Initial perturbations

To investigate the effects of initially-fluctuating magnetic field, we add an ensemble of magnetic field perturbations to the B_y and B_z components in the whole simulation domain as $\delta B_0 = \sum_1^{1024} a(m_x)\cos(\frac{2\pi m_x}{L_x} - \varphi)$, where m_x is the mode number for the *x*-component of the k-vector (k_x), and $a(m_x)$ and $\varphi(m_x)$ are the amplitude of the perturbation and the phase shift for each m_x mode, respectively. $a(m_x)$ is set to be $a(m_x)=a_0({m_x}^s/4^s)^{0.5}$ where a_0 is the amplitude for m_x=4 (near the fastest growing mode of the KH instability [Miura & Pritchett, 1982]) and *s* is the slope of the spectrum (i.e., the spectral index) of the initial fluctuations. $\varphi(m_x)$ is set as $\varphi(m_x) = 0.24191431\times 2\pi m_x$ and $\varphi(m_x) = 0.31142419\times 2\pi m_x$ for B_y ad B_z, respectively, for all modes to be out of phase. Note that this paper considers only the k_x component with constant *s* between m_x=1 and 1024. Effects of the other components as well as more realistic spectral shapes will be investigated in future.

Table 1 shows the set of a_0 and *s* we treated in this paper. Given that turbulent spectra with about -5/3 at MHD-scales were observed in the simulated MMS event in both the magnetosheath and boundary layer, as will be shown in section 4.2, we performed two runs in which *s*=-5/3 with different a_0 (a_0=0.01B_0 for Run-B and a_0=0.001B_0 for Run-C). We also

performed four additional runs in which *s*=-1 (Run-D) and *s*=-1/3 (Run-E) with $a_0=0.01B_0$ and *s*=-11/3 (Run-F) and *s*=-8/3 (Run-G) with $a_0=0.001B_0$, and compared these results with the run with $\delta B_0=0$ (Run-A). The black curves in Figure 1 show 1-D power spectra of the initial B_y fluctuations in the background region for run-B ($\delta B_0^2 \propto k_x^{-5/3}$, $a_0=\delta B_0(m_x=4)=0.01B_0$) and run-C ($\delta B_0^2 \propto k_x^{-5/3}$, $\delta B_0(m_x=4)=0.001B_0$). For both runs, as the simulations proceed, the amplitudes of the modes for small-scales (sub-ion and smaller scales) are damped down to the PIC noise level, while the amplitudes for larger-scales are not significantly changed. Although these background spectra are more or less different from those in the MMS observations (see Figure 12) as well as those in past magnetosheath observations [e.g., Alexandrova et al., 2008], this is the first numerical challenge to investigate the growth of the KH instability in a non-laminar setup in the fully kinetic regime.

3. Simulation results

3.1 Overview of the simulation results

Figures 2 and 3 show the time evolution of 2-D contours of the mixing fraction for ions $F_i=(n_{i1}-n_{i2})/(n_{i1}+n_{i2})$, which highlights the surface of plasma mixing between two regions [e.g., Daughton et al., 2014; Nakamura & Daughton, 2014], for runs-A, B, C and E. For $\delta B_0=0$ (Run-A), the evolution of the surface waves for m_x~4-6 modes, which correspond to the wavelength ($\lambda \sim 4\pi D_0$) of the theoretical fastest growing KH mode in the ideal MHD regime [Miura & Pritchett, 1982], is visibly seen after $t \sim 100\Omega_i^{-1}$. The formation of non-linear vortices of these modes is seen at $t \sim 250\text{-}300\Omega_i^{-1}$ (Figure 2b), and these vortices merge into larger ones in the later time (Figures 2c and 2d). Past MHD and multi-fluid studies suggested that the flow of the non-linear KH vortex locally compresses pre-existing magnetic shear layers and can induce magnetic reconnection [Pu et al., 1990; Knoll & Chacon, 2002; Nakamura et al., 2006, 2008]. Past kinetic simulations further demonstrated that this so-called vortex-induced reconnection (VIR) forms multiple magnetic islands (flux ropes) along the edge of the vortices [Nakamura et al., 2011, 2013]. These islands are merged into the vortex bodies and cause rapid mixing within the vortices as seen in Figures 2c and 2d and recently reported in our kinetic simulations [Nakamura et al., 2011, 2014, 2017a, b].

For run-B ($\delta B_0^2 \propto k_x^{-5/3}$, $\delta B_0(m_x=4)=0.01B$), the evolution of a broad range of modes proceeds faster than those for $\delta B_0=0$ (Figures 2e-2h). In particular, the longer wavelength modes with m_x~2 grow more dominantly than the theoretical fastest growing mode m_x~4-6 modes and are visibly seen even at $t\sim100\Omega_i^{-1}$ (Figure 2e). The vortex structure in the early non-linear phase is more complicated with sub-structures of a broad range of scales than that for $\delta B_0=0$ (compare Figures 2b and 2f). In the later phases, the long wavelength modes with m_x~1-2 grow dominantly (Figure 2g). The growths of these modes are stronger than those for $\delta B_0=0$, leading to formation of a thicker mixing layer than for $\delta B_0=0$ (compare Figures 2d and 2h).

For run-C ($\delta B_0^2 \propto k_x^{-5/3}$, $\delta B_0(m_x=4)=0.001B$), no clear fluctuation is seen at $t=100\Omega_i^{-1}$, and the non-linear vortex structures for the theoretical fastest m_x~4-6 modes dominantly grow at $t=295\Omega_i^{-1}$ (Figures 3a and 3b), as also seen for $\delta B_0=0$. However, unlike in the case of $\delta B_0=0$, the wavy structures for longer wavelength modes are visibly seen at $t=295\Omega_i^{-1}$ (compare Figures 2b and 3b). In the later phases, these long wavelength modes with m_x~1-2 grow more strongly and lead to formation of a thicker mixing layer than $\delta B_0=0$ (compare Figures 2d and 3d). For run-E ($\delta B_0^2 \propto k_x^{-1}$, $\delta B_0(m_x=4)=0.01B$), the overall vortex evolution is similar to Run-B, but smaller-scale modes grow faster than for Run-B (compare Figures 2e-2h and 3e-3h). This could be because the amplitudes of the initial fluctuations for the smaller scale modes for Run-E are larger than those for Run-B.

Figure 4 shows time evolutions of the averaged thickness of the mixing layer in the boundary normal (*y*) direction. For $\delta B_0=0$ (Run-A), the thickness starts increasing after the onset of the VIR in the early non-linear growth phase of the KH instability ($t\sim250\text{-}300\Omega_i^{-1}$). For finite δB_0 with large amplitudes (Runs-B and E), followed by the earlier onset of the KH instability, the mixing starts being enhanced earlier than that for the weak (Run-C) or no δB_0 (Run-A). However, even for the weak δB_0 (Run-C), the mixing progresses faster than that for $\delta B_0=0$ in the later non-linear phases, since the long wavelength modes grow faster than for $\delta B_0=0$.

220 3.2 Mode competition

221 Figure 5 shows time evolutions of 1-D spectra of U_{iy} modes for runs-A, B, C and E
222 (corresponding to the runs shown in Figures 2 to 4). For $\delta B_0=0$ (Figure 5a), the clear peak of the
223 theoretical fastest growing KH mode appears at $m_x\sim5$ at $t\sim150\Omega_i^{-1}$, and then the peak shifts to
224 longer wavelength modes as the vortex merging progresses as seen in Figures 2a-2d. The
225 amplitudes for smaller scale modes are enhanced after $t\sim250\Omega_i^{-1}$ corresponding to the formation
226 of the small-scale island by the VIR.

227 For run-B (Figure 5b), corresponding to the initial fluctuations, larger amplitudes of the
228 U_{iy} fluctuations are seen at longer wavelength modes in the initial phase. A clear peak of the long
229 wavelength modes with $m_x=2$ becomes visible at $t\sim100\Omega_i^{-1}$. Then, the amplitudes for smaller
230 scale modes are enhanced after $t\sim150\Omega_i^{-1}$. After that, the longest wavelength mode ($m_x=1$) is
231 visibly enhanced from $t\sim200\Omega_i^{-1}$. On the other hand, for run-C (Figure 5c) in which the
232 amplitude level of the initial fluctuations is set to be one order of magnitude smaller than for run-
233 B, the amplitudes of the U_{iy} fluctuations are much weaker than for run-B in the initial phase, and
234 start being visibly enhanced at $m_x=2$-8 after $t\sim100\Omega_i^{-1}$. The strong peak of the theoretical fastest
235 growing mode ($m_x\sim5$) appears at $t\sim250$-$300\Omega_i^{-1}$. Then, the peak shifts to the longer wavelength
236 modes and the amplitudes for smaller scale modes are enhanced as seen for run-A. However, the
237 time-scale of the inverse cascade (peak shifting) for run-C is somewhat shorter than that for run-
238 A. The peak amplitude of the longer wavelength modes at $m_x=1$-2 is also somewhat stronger
239 than that for run-A.

240 For run-E (Figure 5d) in which the amplitude level of the initial fluctuations ($a_0=0.01B_0$)
241 is the same as run-B but the spectral index (-1/3) is larger than run-B, the spectrum in the initial
242 phases spreads more widely than run-B. The clear peak near the theoretical fastest growing mode
243 ($m_x\sim4$-5) appears at $t\sim100$-$150\Omega_i^{-1}$. Then, the peak shifts to the longer wavelength modes and the
244 amplitudes for smaller scale modes are enhanced as seen for run-A. However, the time-scale of
245 the inverse cascade for run-E is much (almost two times) shorter than that for run-A. The peak
246 amplitude of the longer wavelength modes at $m_x=1$-2 is also somewhat stronger than that for run-
247 A.

Figure 6, which shows time evolution of the selected U_{iy} modes at m_x=1,2,5 and 10, highlights the differences in the growth of the MHD scale modes seen in Figure 5. For run-A (Figure 6a), a typical inverse cascade process of the KH instability, which corresponds to the vortex merging process as seen in Figures 2a-d, starts from the theoretical fastest growing m_x=5 mode. For run-B (Figure 6b), the longer wavelength m_x=1 and 2 modes are initially enhanced and grow more strongly than the theoretical fastest growing m_x=5 mode. After the initial enhancement of the two modes, the m_x=2 mode dominantly grows, and after t~600Ω_i^{-1} the m_x=1 mode becomes dominant. For run-C (Figure 6c), although the m_x=5 mode grows first as is the case for run-A, the m_x=2 mode starts growing earlier than run-A. As a result, the m_x=2 mode becomes dominant about 50 Ω_i^{-1} earlier than run-A. For run-E (Figure 6d), although the evolution curve of the m_x=2 mode is similar to run-B, the m_x=5 mode dominates until t~200 Ω_i^{-1}. As a result, the inverse cascade from the m_x=5 to 1 modes occurs as in the case of Run-A, but it proceeds about two times faster than run-A. These differences result from the different amplitude of the initial fluctuations for each mode and the resulting mode competitions as below.

The evolution of each mode for δB_0=0 is spontaneously induced by the background random PIC noise. We confirmed that the growth rate of each mode for δB_0=0, measured from the slope of the time evolution of U_{iy}^2 for each mode in the linear growth phase, is consistent with the rate in the ideal MHD regime [Miura & Pritchett, 1982] (not shown). For the finite δB_0, although the growth rate of each mode is not significantly different from the one for δB_0=0 (for example, compare the slopes of the blue curves in Figure 6), the initial magnetic field fluctuations additionally enhance the initial amplitude of the corresponding U_{iy} modes. A similar enhancement of the normal component of the flow velocity in the initial phase is also seen in recent MHD simulations of the KH instability considering flow perturbations for specific modes [Nykyri et al., 2017]. Assuming that the linear growth rate of each U_{iy} mode $\gamma(m_x)$ is the same as the one for δB_0=0, the time-scale $\Delta t(m_x)$ during which the initially enhanced amplitude of a mode $b(m_x)$ grows and reaches a specific level c (~$b \cdot \exp(\gamma \Delta t)$) is described as

$$\Delta t(m_x) \sim \frac{\ln[c/b(m_x)]}{\gamma(m_x)}. \quad (1)$$

Here, we discuss the mode competition between the theoretical fastest growing m_x=5 mode and a longer wavelength m_x=2 mode. Assuming that the initially enhanced amplitude

$b(m_x)$ is proportional to the amplitude of the initial field fluctuation for each mode, defining $b_0=b(5)$, $b(2)=b_0(5/2)^{|s|}$, where s is the spectral index of the initial fluctuations. Since the growth rate for $m_x=5$ is about two times larger than that for $m_x=2$ ($\gamma(2)\sim\gamma(5)/2$) as estimated from the green and blue curves in Figure 6a, using equation (1), the condition in which the $m_x=2$ mode reaches to a specific level c faster than the $m_x=5$ mode (i.e., $\Delta t(2)< \Delta t(5)$) can be described as,

$$\frac{\ln\left[\frac{c}{b_0}\right]-|s|\cdot\ln\left(\frac{5}{2}\right)}{\frac{\gamma(5)}{2}} < \frac{\ln\left[\frac{c}{b_0}\right]}{\gamma(5)}.$$

This relation can be rewritten as,

$$|s| > \frac{\ln\left[\frac{c}{b_0}\right]}{2\ln\left(\frac{5}{2}\right)} \sim \ln\left[\frac{c}{b_0}\right]/2. \quad (2)$$

For runs with $a_0=\delta B_0(m_x=4)=0.01B_0$ (runs-B, D and E), the initial amplitude for $m_x=5$ (i.e., b_0) would be close for all runs. As seen in Figures 6b and 6d, the amplitude of the fluctuations for $m_x=5$ for these runs is enhanced to a level around $b_0^2\sim10^{-7}$-$10^{-6}V_A^2$ in the initial phase. From equation (2), the threshold for the $m_x=2$ mode to reach a certain level $c^2\sim10^{-5}$-$10^{-4}V_A^2$ (shaded levels in Figure 6) faster than the theoretical fastest $m_x=5$ mode can be predicted as $|s|\sim1$. Indeed, as shown in Figure 7a, the $m_x=2$ mode exceeds the $m_x=5$ mode for s=-5/3, both $m_x=2$ and 5 modes reach the shaded level almost at the same time for s=-1, and the $m_x=5$ mode exceeds the $m_x=2$ mode for s=-1/3. In addition, for runs with $a_0=\delta B_0(m_x=4)=0.001B_0$ (runs-C and G) (i.e., runs in which b_0 is set to be one-order of magnitude smaller than the above runs), from equation (2) the threshold can be predicted as $|s|\sim2.5$. And indeed, as shown in Figure 7b, the $m_x=2$ mode exceeds the $m_x=5$ mode for s=-11/3, both modes reach the shaded level almost at the same time for s=-8/3, and the $m_x=5$ mode exceeds the $m_x=2$ mode for for s=-5/3. These results support the adequacy of the prediction from equation (2).

Notice that as seen in Figure 6, once a mode reaches the level of $c^2\sim10^{-5}$-$10^{-4}V_A^2$ first, this mode causes the subsequent inverse cascade - i.e., the modes shorter than this mode can never grow dominantly. Thus, equation (2) suggested that when the amplitude level and the spectral index of the initial fluctuations are sufficiently high and small, respectively, the modes whose wavelengths are longer than the theoretical fastest growing mode can grow more dominantly than the theoretical fastest mode. This may explain the observational features of the

KH waves at the magnetopause, whose wavelengths tend to be longer than the expected wavelength of the theoretical fastest growing mode calculated from the typical thickness of the magnetopause [Hasegawa et al., 2009]. This point will be discussed in section 4.2.

3.3 Spectral evolution

Figure 8a shows averaged 1-D spectra of B_y ($\sim B_\perp$) near the center of the vortex layer over t=0-50 Ω_i^{-1} (initial phase), 100-150 Ω_i^{-1} (onset phase), 150-200 Ω_i^{-1} (early linear phase), 200-250 Ω_i^{-1} (later linear phase), 250-300 Ω_i^{-1} (early non-linear phase), 500-550 Ω_i^{-1} (later non-linear phase), and 750-800 Ω_i^{-1} (final merging phase) for δB_0=0. After the onset of the KH instability, the power near the theoretical fastest growing KH modes (m_x=4-6) is enhanced (see the green to magenta curves). In the early non-linear phase, the power in smaller scale (sub-ion scale) modes starts being enhanced due to the formation of the small-scale islands by the VIR (see the cyan curve). A similar power enhancement at sub-ion scales is also seen in recent kinetic simulations of collisionless plasma turbulence in which reconnection occurs at multiple-points and forms small-scale islands [Franci et al., 2017]. Notice that in this early non-linear phase, the spectrum at MHD scales has not well matured and its spectral index is still near -8/3 as also seen in the past simulation [Nakamura et al., 2017a]. In the later phases, well-matured turbulent spectra with an index close to -5/3 at MHD scales and steeper ones with the minimum index close to -4 at sub-ion scales appear as also seen in past simulations [Daughton et al., 2014; Nakamura et al., 2017a].

For all of the finite δB_0 cases (Figures 8b-d), the spectral indexes in the well-matured phases are close to the ones for δB_0=0 –i.e., ~-5/3 at MHD scales and ~4 or larger at sub-ion scales (see yellow and black lines). However, for finite δB_0, not only the MHD-scale modes but even the sub-ion scale modes grow stronger and earlier than the δB_0=0 case. In particular, for runs-B and E (a_0=0.01B_0), the well-matured turbulent spectra with spectral indexes close to -5/3 at MHD scales form even before the early non-linear phase (before t~250 Ω_i^{-1}) (see magenta curves in Figures 8b and 8d). For run-C (a_0=0.001B_0), the spectral evolution is similar to the one for δB_0=0, although the amplitudes for the MHD-scale modes are slightly stronger especially in the linear phases (compare Figures 8a and 8c). Notice that for run-B (Figure 8b), the spectral

index in the early and later non-linear phases ($t>250\ \Omega_i^{-1}$) is close to -5/3 at MHD scales, -3 at sub-ion scale near k_x~30-100 and -4 at smaller scales (see cyan, yellow and black curves in Figure 8b). This tendency is reasonably consistent with the MMS observations as will be discussed in section 4.2. Notice also that these spectral features for finite δB_0 especially at MHD and sub-ion scales are not significantly affected by m_i/m_e as seen in Figure 9a which shows the spectra for the case with the same setting as run-B (Figure 8b) but for m_i/m_e=100 and the corresponding two times smaller grid spacing. However, at sub-ion and smaller scales, the transition range in the spectra where the index is about -3 is somewhat wider for m_i/m_e=100 (compare red and blue curves in Figure 9b). This indicates that the transition from -3 to -4 slopes could be affected by electron dynamics. The spectrum formation processes at the sub-ion to electron scales will be investigated in more detail in future.

Figure 10 shows the spectra of $|\mathbf{B}|$ and B_y (~$B_\perp$) for run-A (top) and B (bottom). For both runs, there is a clear tendency that the fluctuations develop dominantly in the perpendicular direction in both MHD and sub-ion scales. The difference between $|\mathbf{B}|$ and B_y at both scales increases with time, and the power of B_y becomes more than one order larger than that of $|\mathbf{B}|$ at both scales in the well-matured phases. This is because both the KH instability at MHD-scales and the subsequent VIR at sub-ion scales evolve mainly in the perpendicular direction. This tendency is also reasonably consistent with past spacecraft observations of the KH waves at the magnetopause as will be discussed in Section 4.2.

4. Summary and Discussion

4.1 Summary

We have performed a series of 2-D fully kinetic simulations of the MMS event on 8 September 2015, in which the non-linear KH waves and clear signatures of the vortex-induced reconnection (VIR) were observed [Eriksson et al., 2016a; Nakamura et al., 2017a,b], newly considering initially-fluctuating magnetic field. The main results of this paper are summarized as follows:

360 1. For the initial field fluctuations, we add an ensemble of k_x modes with different
361 amplitudes to form a power-law spectrum. When the initial amplitude of a mode exceeds
362 the PIC noise level, the mode starts growing from the level of the initial perturbation.

363 2. In consequence of the competition among modes having different initial amplitudes, the
364 longer wavelength modes can grow dominantly, as the amplitude level and spectral index
365 of the initial fluctuations become higher and smaller, respectively.

366 3. For finite δB_0, the growth time-scale of the KH instability is small compared to the no
367 δB_0 case, leading to a more efficient plasma mixing within the vortex layer.

368 4. For large δB_0, the power of spectra is enhanced especially for the $B_\perp$ component over
369 sub-ion to MHD scales, and the well-matured spectrum with a -5/3 index can be seen
370 even in the early non-linear growth phase of the KH instability.

371

372 4.2 Comparison with observations

373 Figure 11 shows averaged power spectra of $|\mathbf{B}|$ and $B_\perp$ in the MMS observations on 8
374 September 2015 over the KH wave intervals and the adjacent magnetosheath interval (just after
375 the wave interval). The wave intervals employed here (Figures 11a and 11b) are the same as the
376 ones employed in Stawarz et al. [2016]. The magnetosheath interval is nearly the same as the one
377 used in the simulations of this event to obtain the initial simulation parameters on the
378 magnetosheath side in the previous (Nakamura et al. [2017a,b]) and present simulations. The
379 averaged magnetic field strengths of the wave and magnetosheath intervals are 70 nT and 75 nT,
380 respectively. The turbulent spectrum with an index close to -5/3 at MHD scales was observed
381 during the wave interval (Figure 11a), which was not seen in the early non-linear phase in the
382 past and present simulations with $\delta B_0=0$ (see the cyan curve in Figure 8a and Figure 2 in
383 Nakamura et al. [2017a]). The power of the observed spectra for $B_\perp$ at both MHD and sub-ion
384 scales was more than one-order larger than that for $|\mathbf{B}|$ (Figure 11b). The observed spectral index
385 for $B_\perp$ at sub-ion scales (~1-100 Hz) is somewhat larger than -4 (close to -3), while that at
386 smaller-scales (above ~100 Hz) is close to -4. These points are reasonably consistent with the
387 present simulations for run-B in the early non-linear phase (see cyan curves in Figures 10c and
388 10d).

389 The turbulent spectra were also observed during the adjacent magnetosheath interval of
390 this MMS event (Figures 11a and 11b), as reported in past magnetosheath observations [e.g.,
391 Alexandrova et al. 2008; Roberts et al., 2018]. A similar spectrum (the slope and the relative
392 amplitudes considering the background field strengths) was also observed during the adjacent
393 boundary layer interval of this event (not shown). In the simulation for run-B, the power of the
394 B_y ($\sim B_\perp$) fluctuations near the center of the vortex layer is one or two order larger than that in the
395 background region over ion-scales to MHD scales (compare the cyan curve in Figure 10c and the
396 blue solid curve in Figure 1). Although the observed spectra in the magnetosheath (black curves
397 in Figure 11) is not perfectly reproduced in the simulation, this spectral feature for run-B is
398 reasonably consistent with the observed relative enhancement of the $B_\perp$ fluctuations in the wave
399 interval compared to the magnetosheath interval in this MMS event (see Figures 11b). These
400 consistencies on the spectral features between the simulation for run-B and the MMS
401 observations suggest that the effects of fluctuating magnetic field on the vortex layer as seen in
402 the present simulations for large δB_0 may really occur during this MMS event.

403 Figure 12 shows averaged power spectra of $|\mathbf{B}|$ and $B_\perp$ in the Geotail-Cluster conjunctive
404 observation event on 20 November 2001, which was reported in Hasegawa et al. [2009], over the
405 KH wave interval for Geotail (19:20-19:35 UT) and Cluster (19:20-19:35 UT) and the adjacent
406 magnetosheath interval for Geotail (19:00-19:15 UT). In this event, Geotail, located at the
407 postnoon (~15MLT) magnetopause, and Cluster, located at the dusk-flank (~19MLT)
408 magnetopause, simultaneously observed quasi-periodic KH waves. Hasegawa et al. [2009]
409 suggested that the growth phase of the observed KH waves at the Cluster location was in a range
410 of the non-linear phase, while that at the Geotail location was in a much earlier phase (probably,
411 onset to linear phases). The averaged magnetic field strengths of the wave and magnetosheath
412 intervals are 40.9 nT (Geotail, wave), 20.6 nT (Cluster, wave) and 24,4 nT (Geotail, sheath),
413 respectively. Considering these field strengths during the observed intervals, the relative
414 amplitude of the $B_\perp$ spectrum observed by Geotail during the KH wave intervals compared to
415 that during the magnetosheath interval was about one order larger than the relative amplitude of
416 the $|\mathbf{B}|$ spectrum (see Figure 12a and 12c) especially at the MHD scales, as seen in the simulation
417 for run-B in the linear phase (compare red and blue curves in Figures 10c and 10d). This
418 indicates that the $B_\perp$ fluctuations were enhanced by the KH instability, as also seen in the above
419 MMS event. In addition, considering the background field strengths (i.e., normalized by the field

strengths), the relative $B_\perp$ amplitude during the wave interval especially at the MHD scales at the Cluster location was about five times larger than that at the Geotail location (see Figure 12d). This indicates that the field fluctuations within the vortex layer were additionally enhanced as the KH instability traveled and evolved along the magnetopause as seen in the present simulations. Furthermore, while the observed spectral index for $B_\perp$ at sub-ion scales at the Geotail location was somewhat larger than -4, that at the Cluster locations was close to -4 (see Figure 12d). These spectral features are roughly consistent with the present simulations (see Figure 10c), although the relative fluctuations in the magnetosheath compared to the KH wave intervals in this Geotail-Cluster event are somewhat stronger than those in the above MMS event as well as the present simulations.

In addition, in this Geotail-Cluster event, Hasegawa et al. [2009] reported that the observed wavelength of the KH waves ($>4\times10^4$ km) was a few times longer than the one for the theoretical fastest growing KH mode calculated from the thickness of the velocity shear layer ($\sim10^3$ km). This point is also reasonably consistent with the present simulation for run-B, in which the m_x=2 mode dominantly grows first and cascades to the m_x=1 mode, and consequently the theoretical fastest growing m_x=4-5 mode never exceeds these longer wavelength modes. All of these consistencies between the present simulation for finite δB_0 (especially for run-B) and the observations naturally suggest that the magnetic field fluctuations as observed in the magnetosheath and boundary layer may really affect the subsequent evolution of the KH instability at the magnetopause.

Note that the simulations performed in this study setup the constant spectral indices in the initial state, despite the observed spectra near the magnetopause commonly feature smaller indices at sub-ion and smaller scales as seen in Figures 11 and 12. This may lead to a stronger evolution of the small-scale modes than the case with a non-constant index. Thus, to more quantitatively comparae the simulations with the observations, more realistic initial fluctuations need to be setup by considering the nonconstant spectral index, as well as the k_y and k_z modes, which are also not considered in this study. In addition, although this paper sets up the initial fluctuations only in the magnetic field, strong fluctuations in plasma parameters such as flow velocity have also been frequently observed in the magnetosheath [e.g., Plaschke et al., 2019]. Although the present simulations showed that initial magnetic field fluctuations immediately

enhance the velocity fluctuations (see section 3.2), setting up the initial fluctuations even in the flow velocities as well as the other parameters such as density may also be important to discuss the effects of the background turbulence more quantitatively. Furthermore, since spectral features of the background turbulence, such as slopes and amplitudes at each scale, are variable depending on various factors such as the plasma β [e.g., Alexandrova et al., 2008], to more comprehensively understand how strongly the background turbulence affects the KH instability at the magnetopause, it will be needed to statistically analyze more events at different locations under different conditions. Based on the initial studies shown in this paper, such more practical approaches in both simulation and observation may lead to a more realistic and quantitative understanding of the roles of the KH instability at the magnetopause.

4.3 Some other remarks on future work

Although this study treats only 2-D simulations, recent 3-D fully kinetic simulations of the KH instability showed the importance of the 3-D effects especially on the formation of the secondary flux ropes [Nakamura et al., 2013; 2017a,b]. These simulations demonstrated that in 3-D, the VIR can be induced over a range of oblique angles, leading to a more turbulent formation of the flux ropes within the vortex layer. Recent 3-D two-fluid simulations also showed that when considering a more realistic magnetopause-like situation in which the low-latitude unstable region of the KH instability is sandwiched between the high-latitude stable regions, the VIR can be induced even in the mid-latitude region where the growth of the KH instability is much weaker than the low-latitude region [e.g., Fadanelli et al., 2018]. Moreover, recent 3-D fully kinetic simulations of the magnetopause demonstrated that the density jump across the magnetopause can potentially cause electromagnetic turbulence induced by the lower-hybrid drift instability (LHDI) [Price et al., 2016; Le et al., 2017]. Such an LHDI turbulence at the magnetopause would also be coupled with the KH instability under certain conditions. Indeed, intense LHD waves were recently observed by MMS within the KH instability at the magnetopause [Tang et al., 2018]. Investigating the coupling of these 3-D effects with the background turbulence is an important direction for future research.

As mentioned in section 3.3, the formation of spectral slopes including sub-ion and smaller scales may be affected by the VIR and the resulting turbulent formation of the magnetic

480 islands within the vortex layer. Based on hybrid (ion kinetic and mass-less electron fluid)
481 simulations, Franci et al. [2017] suggested that the turbulent formation of small-scale islands can
482 produce an inverse cascade through the island merging in addition to the direct cascade through
483 the island formation. This two-way cascade leads to the formation of the spectrum with a ~-3
484 index at sub-ion scales, which is reasonably consistent with the present simulation as seen in
485 Figures 9b. Past fully kinetic simulations demonstrated that in the VIR process, reconnection is
486 first induced at compressed current layers whose thicknesses are of the order of d_e [Nakamura et
487 al., 2011; 2013], indicating that the two-way cascade as seen in Franci et al. [2017] would occur
488 even at electron scales in the fully kinetic regime. On the other hand, past theories suggested that
489 electron flow turbulence in the direction perpendicular to the magnetic field can cause additional
490 energy cascade from MHD to electron scales and form the spectrum with a -4 or smaller index at
491 electron scales [e.g., Narita, 2016]. The secondary turbulence within the vortex layer may drive
492 additional reconnection as seen in the magnetosheath turbulence [e.g., Retinò et al. 2007;
493 Yordanova et al. 2016; Vörös et al. 2017; Phan et al. 2018; Stawarz et al. 2019], which may also
494 contribute to energy dissipation and plasma mixing and/or influence the small-scale non-linear
495 dynamics. Investigating such sub-ion to electron scale physics related to the KH instability and
496 understanding which processes dominantly transfer energies at these scales are also an important
497 direction for future research.

498 Finally, since it is known that the field and flow fluctuations tend to be stronger in the
499 dawnside magnetosheath (i.e., in the downstream of the quasi-parallel shock for the solar wind
500 Parker spiral), the effects of turbulent fluctuations on the KH instability as seen in the present
501 simulations may be more important at the dawnside magnetopause [e.g., Luhmann et al., 1986;
502 Plaschke et al., 2019]. For example, Moore et al. [2016] showed an observation event of the KH
503 waves at the dawn-flank magnetopause in which the cold ions were effectively heated by ion-
504 scale waves within the KH waves. Although it is difficult to treat these global pictures in the
505 fully kinetic regime, global hybrid (fluid-electron and kinetic-ions) simulations, which recently
506 began to be applied for the whole Earth's magnetosphere [Palmroth et al., 2018 and references
507 therein], may provide important support for treating such global physics of the magnetosheath
508 turbulence and its relation to the KH instability at the magnetopause.

509

6. Conclusions

We have performed a series of 2-D fully kinetic simulations of an MMS observation event on 8 September 2015, in which the non-linear KH waves were observed at the Earth's magnetopause, considering the pre-existing turbulent magnetic field fluctuations. This is the first numerical challenge to investigate the effects of fluctuating magnetic field on the growth of the KH instability at the magnetopause in the fully kinetic regime. Here we setup the initial fluctuations by adding an ensemble of k_x modes to the magnetic field and perform runs changing the amplitude level and the spectral index of the fluctuations. The results demonstrate (i) that when the amplitude level is sufficiently high, the initial fluctuations can cause a faster evolution of the KH instability, leading to a more efficient plasma mixing within the vortex layer, and (ii) that longer wavelength modes grow more dominantly as the spectral index becomes smaller with negative sign. For the cases with large amplitude of the initial fluctuations, the well-matured spectrum with a -5/3 index appears even in the early non-linear growth phase of the KH instability. These simulation results are reasonably consistent with the observations in this MMS event and a past Geotail-Cluster conjunction event in which Geotail and Cluster observed the KH waves at the postnoon and dusk-flank magnetopause, respectively. Based on these initial results, future researches with more realistic approaches, for example, by setting more realistic spectral signatures of the initial fluctuations may lead to a more quantitative understanding of the effects of the background turbulence on the evolution of the sheared boundary at the magnetopause.

Acknowledgments

This work was supported by the Austrian Research Fund (FWF): I2016-N20. JES is supported by UKRI/STFC grant ST/S000364/1. For the simulations employed in this paper, we acknowledge PRACE for awarding us access to MareNostrum at Barcelona Supercomputing Center (BSC), Spain. A part of the simulation data was analyzed with resources at the Space Research Institute of Austrian Academy of Sciences. The observational portion of this research uses data from the MMS spacecraft. The MMS data are publically available via NASA resources and the Science Data Center at CU/LASP (https://lasp.colorado.edu/mms/sdc/public/). Geotail data are publicly available from DARTS/Geotail (https://darts.isas.jaxa.jp/stp/geotail/). Cluster data are publicly available from the Cluster Science Archive

(https://www.cosmos.esa.int/web/csa) (Laakso et al., 2010). We especially thank W. Daughton for his support to setup the VPIC simulations performed in this paper.

References

Alexandrova, O., C. Lacombe, A. Mangeney, Spectra and anisotropy of magnetic fluctuations in the Earth's magnetosheath: Cluster observations (2008), *Ann. Geophys.* 26, 3585-3596.

Balogh, A., et al. (2001), The Cluster magnetic field investigation: Overview of in-flight performance and initial results, Ann. Geophys., 19, 1207–1217.

Bowers, K. J., B. J. Albright, L. Yin, B. Bergen, and T. J. T. Kwan (2008), Ultrahigh performance three-dimensional electromagnetic relativistic kinetic plasma simulation, *Phys. Plasmas* **15**, 055703.

Bowers, K. et al (2009). Advances in petascale kinetic simulations with VPIC and Roadrunner, *J. Phys.: Conf. Series* **180**, 012055.

Burch, J. L., T. E. Moore, R. B. Torbert, and B. L. Giles (2016), Magnetospheric Multiscale overview and science objectives, Space Sci. Rev., 199, 5–21 doi:10.1007/s11214-015-0164-9.

Daughton, W., T. K. M. Nakamura, H. Karimabadi, V. Roytershteyn, and B. Loring (2014), Computing the reconnection rate in turbulent kinetic layers by using electron mixing to identify topology, *Physics of Plasmas* **21**, 052307.

Dungey, J. W. (1955), Electrodynamics of the outer atmosphere, in Proceedings of the Conference of the Ionosphere, 255 pp., Phys. Soc. of London, London, U. K.

Eriksson, S. et al. (2016a), Magnetospheric Multiscale observations of magnetic reconnection associated with Kelvin-Helmholtz waves, *Geophys. Res. Lett.*, 43, 5606-5615, doi:10.1002/2016GL068783.

Eriksson, S. et al. (2016b), Magnetospheric Multiscale Observations of the Electron Diffusion Region of Large Guide Field Magnetic Reconnection, *Phys. Rev. Lett.* 117, 015001.

Fadanelli, S., Faganello, M., Califano, F., Cerri, S. S., Pegoraro, F., & Lavraud, B. (2018). North-south asymmetric Kelvin-Helmholtz instability and induced reconnection at the Earth's magnetospheric flanks. *Journal of Geophysical Research: Space Physics*, 123, 9340– 9356. https://doi.org/10.1029/2018JA025626

Fairfield, D. H., and A. Otto, et al. (2000), Geotail observations of Kelvin-Helmholtz instability at the equatorial magnetotail boundary for parallel northward fields, *J. Geophys. Res.*, **105**, 21,159, doi:10.1029/1999JA000316.

Foullon, C., C. J. Farrugia, A. N. Fazakerley, C. J. Owen, F. T. Gratton, and R. B. Torbert (2008), Evolution of Kelvin-Helmholtz activity on the dusk flank magnetopause, J. Geophys. Res., 113, A11203, doi:10.1029/2008JA013175.

Franci, L., Silvio Sergio Cerri, Francesco Califano, Simone Landi, Emanuele Papini, Andrea Verdini, Lorenzo Matteini, Frank Jenko and Petr Hellinger (2017), Magnetic Reconnection as a Driver for a Sub-ion-scale Cascade in Plasma Turbulence, The Astrophysical Journal, 850(1), L16, doi:10.3847/2041-8213/aa93fb

Hasegawa, H., et al. (2004), Transport of solar wind into Earth's magnetosphere through rolled-up Kelvin-Helmholtz vortices, *Nature*, **430**, 755, doi:10.1038/nature02799.

Hasegawa, H., M. Fujimoto, K. Takagi, Y. Saito, T. Mukai, and H. Re`me (2006), Single-spacecraft detection of rolled-up Kelvin-Helmholtz vortices at the flank magnetopause, *J. Geophys. Res.*, *111*, A09203, doi:10.1029/2006JA011728.

Hasegawa, H., et al. (2009), Kelvin-Helmholtz waves at the Earth's magnetopause: Multiscale development and associated reconnection, J. Geophys. Res., 114, A12207, doi:10.1029/2009JA014042.

Kavosi, S. and J. Raeder (2015), Ubiquity of Kelvin–Helmholtz waves at Earth's magnetopause. Nat. Commun. 6:7019 doi: 10.1038/ncomms8019.

Kivelson, M. G., and S.-H. Chen (1995), The magnetopause: Surface waves and instabilities and their possible dynamic consequences, in *Physics of the Magnetopause, Geophys. Monogr. Ser.*, vol. 90, edited by P. Song et al., 257 pp., AGU, Washington, D. C.

Kokubun, S., H. Kawano, M. Nakamura, T. Yamamoto, K. Tsuruda, H. Hayakawa, A. Matsuoka, and L. A. Frank (1994), Quasi-periodic oscillations of the magnetopause during northward sheath magnetic field, Geophys. Res. Lett., 21, 2883–2886.

Laakso, H., C. Perry, S. McCaffrey, D. Herment, A.J. Allen, C.C. Harvey, C.P. Escoubet, C. Gruenberger, M.G.G.T. Taylor, and R. Turner (2010). Cluster Active Archive: Overview, 3-37, The Cluster Active Archive, Astrophysics and Space Science Proceedings, H. Laakso et al. (eds.), Springer.

Le, A., W. Daughton, L.-J. Chen, and J. Egedal (2017), Enhanced electron mixing and heating in 3-D asymmetric reconnection at the Earth's magnetopause, *Geophys. Res. Lett.* **44**, 2096

Le Contel, O., et al. (2016), The search-coil magnetometer for MMS, Space Sci. Rev., 199, 257-282, doi:10.1007/s11214-014-0096-9.

Li, W., et al. (2016), Kinetic evidence of magnetic reconnection due to Kelvin-Helmholtz waves, *Geophys. Res. Lett.*, **43**, 5635–5643, doi:10.1002/2016GL069192.

Luhmann, J. G., C. T. Russell, and R. C. Elphic (1986), Spatial distributions of magnetic field fluctuations in the dayside magnetosheath, J. Geophys. Res., 91(A2), 1711–1715, doi:10.1029/JA091iA02p01711.

Matsumoto, Y., and K. Seki (2010), Formation of a broad plasma turbulent layer by forward and inverse energy cascades of the Kelvin–Helmholtz instability, J. Geophys. Res., 115, A10231, doi:10.1029/2009JA014637.

Miura, A., and P. L. Pritchett (1982), Nonlocal stability analysis of the MHD Kelvin-Helmholtz instability in a compressible plasma, *J. Geophys. Res.*, **87**, 7431-7444.

Moore, T. W., K. Nykyri, and A. P. Dimmock (2016), Cross-scale energy transport in space plasmas, Nature Physics, 12, 1164-1169

Nakamura, T. K. M., M. Fujimoto, and A. Otto (2006), Magnetic reconnection induced by weak Kelvin-Helmholtz instability and the formation of the low-latitude boundary layer, Geophys. Res. Lett., 33, L14106, doi:10.1029/2006GL026318.

Nakamura, T. K. M., M. Fujimoto, and A. Otto (2008), Structure of an MHD-scale Kelvin-Helmholtz vortex: Two-dimensional two-fluid simulations including finite electron

622 inertial effects, *Journal of Geophysical Research*, **113**, A09204,
623 doi:10.1029/2007JA012803.

624 Nakamura, T. K. M., H. Hasegawa, I. Shinohara, and M. Fujimoto (2011), Evolution of an
625 MHD-scale Kelvin-Helmholtz vortex accompanied by magnetic reconnection: Two-
626 dimensional particle simulations, *Journal of Geophysical Research*, **116**, A03227,
627 doi:10.1029/2010JA016046.

628 Nakamura, T. K. M., W. Daughton, H. Karimabadi, and S. Eriksson (2013), Three-dimensional
629 dynamics of vortex-induced reconnection and comparison with THEMIS observations,
630 *Journal of Geophysical Research*, **118**, 5742-5757, doi:10.1002/jgra.50547.

631 Nakamura, T. K. M., and W. Daughton (2014)., Turbulent plasma transport across the Earth's
632 low-latitude boundary layer, *Geophysical Research Letters*, **41**, 8704-8712,
633 doi:10.1002/2014GL061952.

634 Nakamura, T. K. M., R. Nakamura, Y. Narita, W. Baumjohann, and W. Daughton (2016), Multi-
635 Scale Structures of Turbulent Magnetic Reconnection, *Physics of Plasmas*, **23**, 052116,
636 doi:10.1063/1.4951025.

637 Nakamura, T. K. M., H. Hasegawa, W. Daughton, S. Eriksson, W. Y. Li, and R. Nakamura
638 (2017a), Turbulent mass transfer caused by vortex-induced reconnection in collisionless
639 magnetospheric plasmas, *Nature Communications*, 8, 1582.

640 Nakamura, T. K. M., Eriksson, S., Hasegawa, H., Zenitani, S., Li, W. Y., Genestreti, K. J., et al.
641 (2017b). Mass and energy transfer across the Earth's magnetopause caused by vortex-
642 induced reconnection. Journal of Geophysical Research: Space Physics, 122, 11,505–
643 11,522. https://doi.org/10.1002/2017JA024346

644 Nakamura, T. K. M. (2019), the Earth's low-latitude boundary layer, accepted *in*
645 *"Solar/heliosphere 2, Magnetospheres of the solar system" (AGU Book)*, Wiley

646 Narita, Y (2016), Kinetic extension of critical balance to whistler turbulence, The Astrophysical
647 Journal, 831, 83.

648 Nykyri, K., X. Ma, A. Dimmock, C. Foullon, A. Otto, and A. Osmane (2017), Influence of
649 velocity fluctuations on the Kelvin-Helmholtz instability and its associated mass
650 transport, *J. Geophys. Res. Space Physics*, *122*, 9489–9512, doi:10.1002/2017JA024374.

Palmroth, M., U., Ganse, Y., Pfau-Kempf et al. (2018), Vlasov methods in space physics and astrophysics, Living Rev. Comput. Astrophys. 4, 1, https://doi.org/10.1007/s41115-018-0003-2.

Phan, T. D., Eastwood, J. P., Shay, M. A., Drake, J. F., Sonnerup, B., Fujimoto, M., and et al. (2018). Electron magnetic reconnection without ion coupling in earth's turbulent magnetosheath. Nature 557, 202–206. doi: 10.1038/s41586-018-0091-5.

Price, L., M. Swisdak, J. F. Drake, P. A. Cassak, J. T. Dahlin, and R. E. Ergun (2016), The effects of turbulence on three-dimensional magnetic reconnection at the magnetopause, *Geophys. Res. Lett.*, *43*, 6020–6027, doi:10.1002/2016GL069578.

Pritchett, P. L., and F. V. Coroniti (1984), The collisionless macroscopic Kelvin-Helmholtz instability 1: Transverse electrostatic mode, *J. Geophys. Res.*, **89**, 168–178.

Retino, A., Sundkvist, D., Vaivads, A., Mozer, F., Andre, M., and Owen, C. (2007). In situ evidence of magnetic reconnection in turbulent plasma. Nat. Phys. 3, 235–238. doi: 10.1038/nphys574.

Roberts, O. W., Toledo-Redondo, S., Perrone, D., Zhao, J., Narita, Y., Gershman, D., et al. (2018). Ion-scale kinetic Alfven turbulence: MMS measurements of the Alfven ratio in the magnetosheath. *Geophysical Research Letters*, *45*, 7974–7984. https://doi.org/10.1029/2018GL078498

Russell, C. T., et al. (2016), The Magnetospheric Multiscale magnetometers, Space Sci. Rev., 199, 189-256, doi:10.1007/s11214-014-0057-3.

Sckopke, N. G., G. Paschmann, G. Haerendel, B. U. O. Sonnerup, S. J. Bame, T. G. Forbes, E.W. Hones Jr., and C. T. Russell (1981), Structure of the lowlatitude boundary layer, J. Geophys. Res., 86, 2099–2110.

Slinker, S. P., J. A. Fedder, D. G. Sibeck, J. G. Lyon, L. A. Frank, and T. Mukai (2003), Simulation of magnetopause oscillations observed January 9, 1996, Geophys. Res. Lett. 30(11), 1569, doi:10.1029/ 2003GL017063.

Stawarz, J. E., et al. (2016), Observations of turbulence in a Kelvin-Helmholtz event on 8 September 2015 by the Magnetospheric Multiscale mission, *J. Geophys. Res. Space Physics*, *121*, 11,021–11,034, doi:10.1002/2016JA023458.

Stawarz, J. E., Eastwood, J., Phan, T., Gingell, I., Shay, M., Burch, J., et al. (2019). Properties of the turbulence associated with electron-only magnetic reconnection in earths magnetosheath. Astrophys. J. Lett. 877, 1–7. doi: 10.3847/2041-8213/ab21c8.

Sturner, A. P., Eriksson, S., Nakamura, T., Gershman, D. J., Plaschke, F., Ergun, R. E., et al. (2018). On multiple Hall-like electron currents and tripolar guide magnetic field perturbations during Kelvin-Helmholtz waves. Journal of Geophysical Research: Space Physics, 123, 1305–1324. https://doi.org/10.1002/2017JA024155

Tang, B., Li, W., Wang, C., Dai, L., Khotyaintsev, Y., Lindqvist, P.-A., Ergun, R., Le Contel, O., Pollock, C., Russell, C., and Burch, J. (2018), Magnetic depression and electron transport in an ion-scale flux rope associated with Kelvin–Helmholtz waves, Ann. Geophys., 36, 879-889, https://doi.org/10.5194/angeo-36-879-2018.

Vernisse, Y. et al. (2016), Signatures of complex magnetic topologies from multiple reconnection sites induced by Kelvin-Helmholtz instability, *Journal of Geophysical Research,* doi:10.1002/2016JA023051.

Vörös, Z., Yordanova, E., Varsani, A., Genestreti, K., Khotyaintsev, Y., Li, W., et al. (2017). MMS observation of magnetic reconnection in the turbulent magnetosheath. J. Geophys. Res. Space Phys. 122, 11442–11467.

Yordanova, E., Vörös, Z., Varsani, A., Graham, D., Norgren, C., Khotyainstev, Y., et al. (2016). Electron scale structures and magnetic reconnection signatures in the turbulent magnetosheath. Geophys. Res. Lett. 43, 5969–5978. doi: 10.1002/2016GL069191.

701 **Table-1.** *s* (the spectral index of δB_0^2) and a_0 (=δB_0 for m_x=4) employed in the simulations
702 shown in this paper.

Run	A	B	C	D	E	F	G
s	N/A	-5/3	-5/3	-1	-1/3	-11/8	-8/3
a_0/B_0	0	0.01	0.001	0.01	0.01	0.001	0.001

703

704

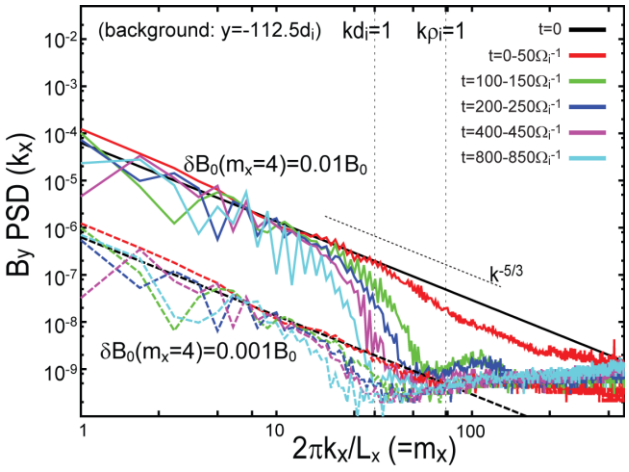

Figure 1. 1-D power spectra (k_x) of B_y in the background on the higher-density side (y=-112.5±14.6 d_i) for run-B ($\delta B_0^2 \propto k_x^{-5/3}$, $\delta B_0(m_x=4)=0.01B_0$) and run-C ($\delta B_0^2 \propto k_x^{-5/3}$, $\delta B_0(m_x=4)=0.001B_0$) at t=0 (initial) and averaged over t=0-50 Ω_i^{-1}, 100-150 Ω_i^{-1}, 200-250 Ω_i^{-1}, 400-450 Ω_i^{-1}, 800-850 Ω_i^{-1}. The vertical lines in Figure 1b indicate the wavelengths for $k_\perp \rho_i = 1$ and $k_\perp d_i = 1$.

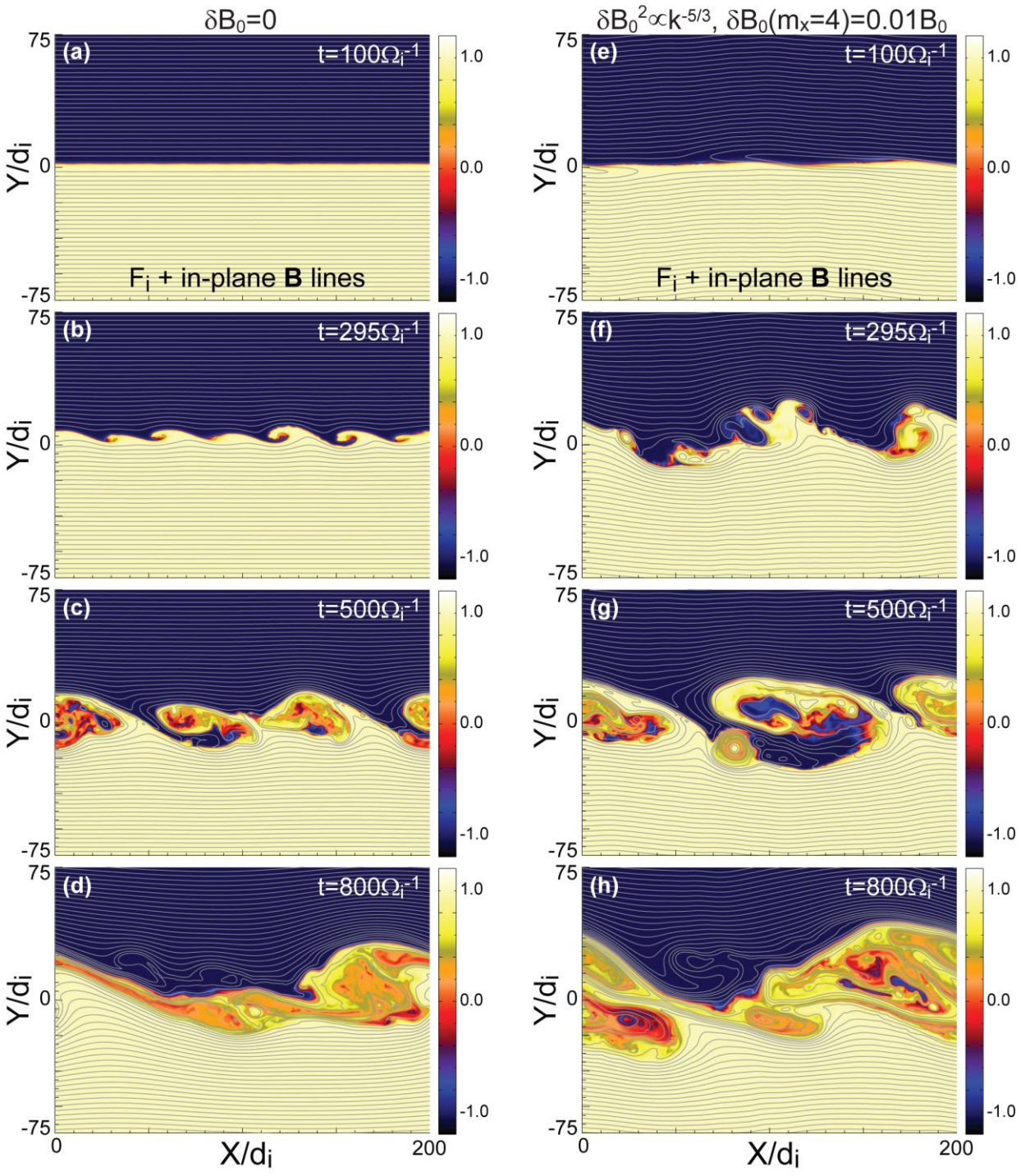

711

712 **Figure 2.** Time evolution from the linear (a,e) to the late non-linear (d,h) growth phase of the
713 KH instability of 2-D contours of the ion mixing fraction F_i for run-A (δB_0=0) (a-d) and run-B
714 ($\delta B_0^2 \propto k_x^{-5/3}$, $\delta B_0(m_x=4)=0.01B_0$) (e-h). Grey curves show in-plane magnetic field lines.

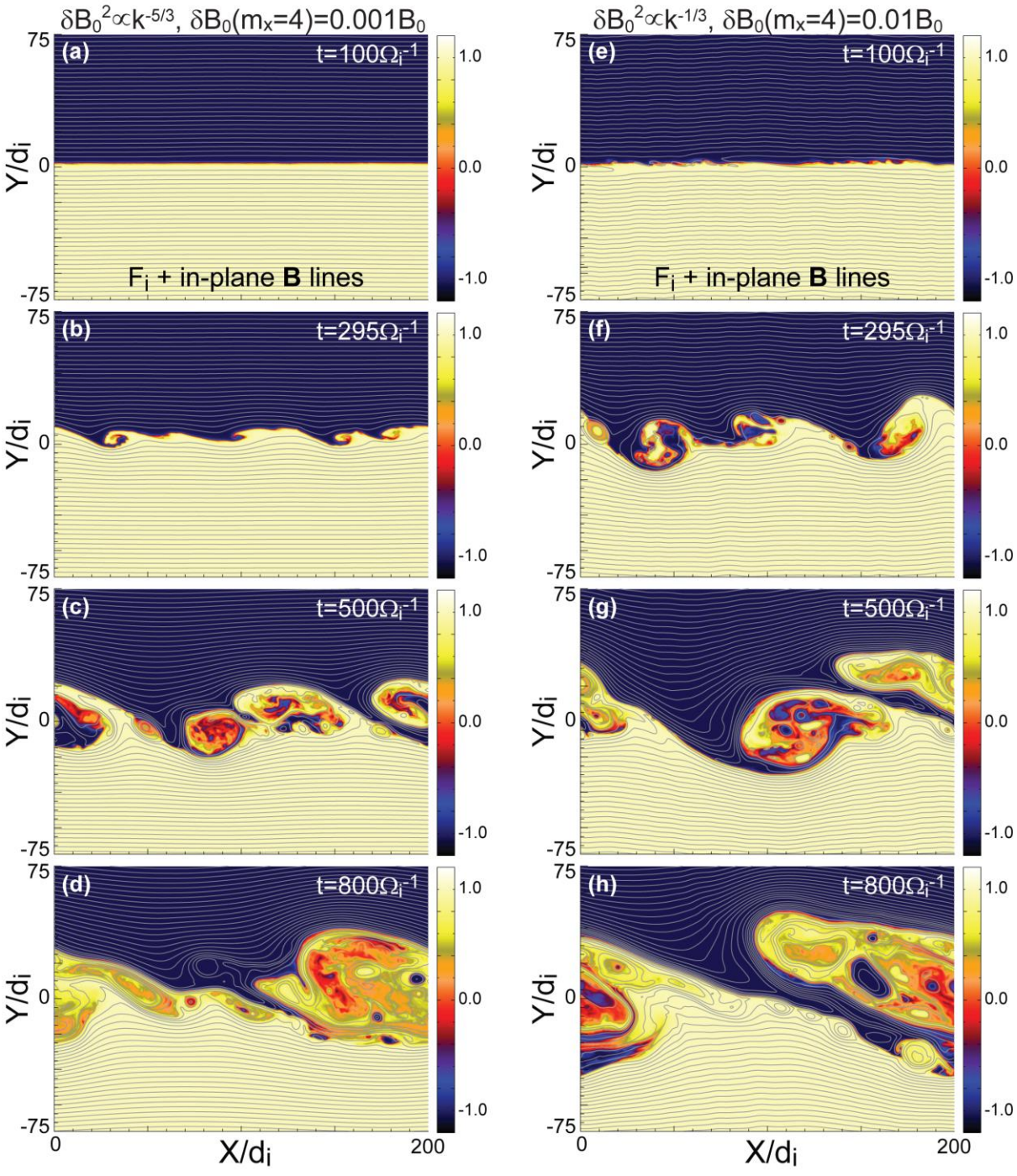

715

716 **Figure 3.** The same as Figure 2, but for run-C ($\delta B_0^2 \propto k_x^{-5/3}$, $\delta B_0(m_x=4)=0.001B_0$) (a-d) and run-

717 E ($\delta B_0^2 \propto k_x^{-1/3}$, $\delta B_0(m_x=4)=0.01B_0$) (e-h).

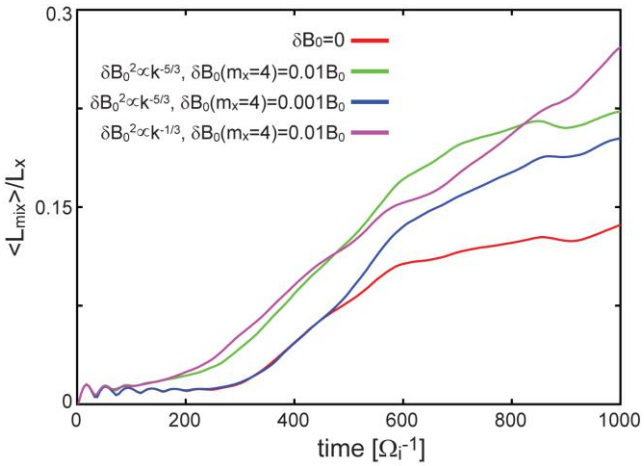

718

719 **Figure 4.** Time evolution of the averaged thickness $<L_{mix}>$ of the mixing layer (defined by the
720 region with $|F_i|<0.9$) in the *y*-direction for runs-A (red), B (green), C (blue) and E (magenta).

721

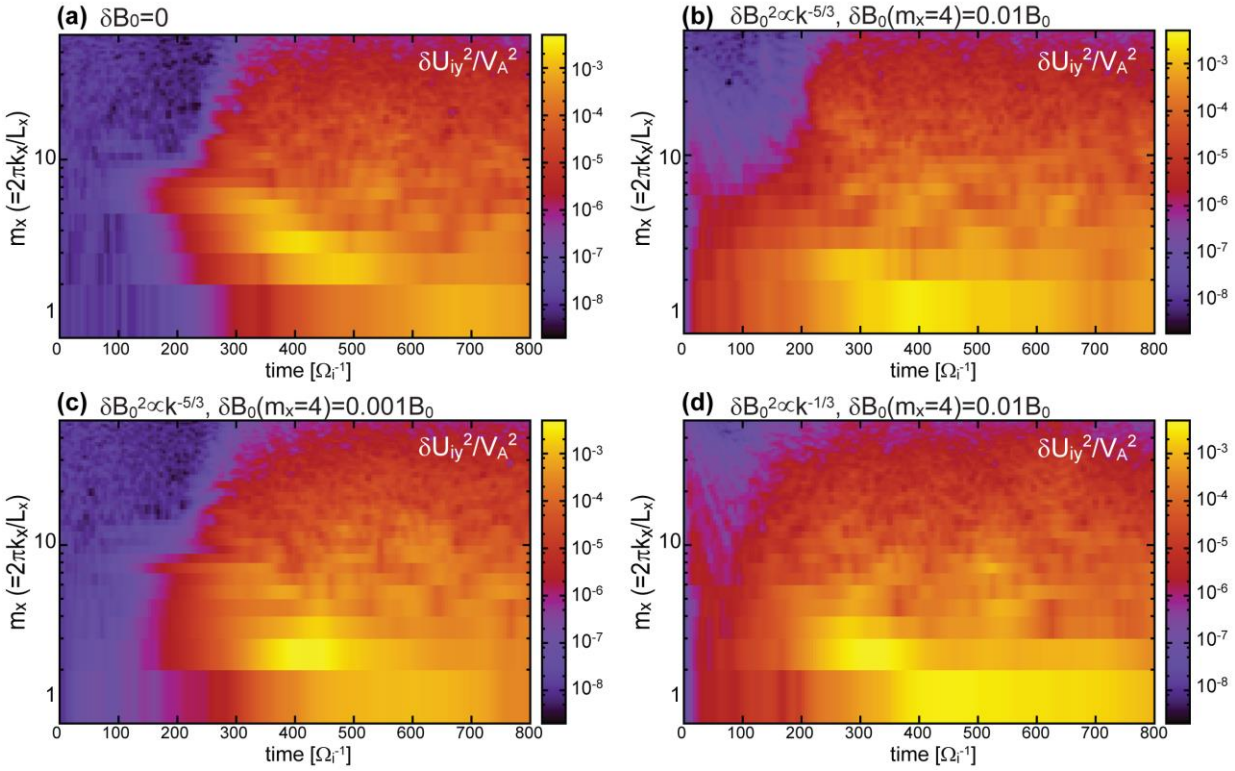

722

723 **Figure 5.** Time evolution of the 1-D power spectra (k_x) of U_{iy} modes around the center of the

724 boundary (y=0±14.6d_i) for runs-A (a), B (b), C (c) and E (d).

725

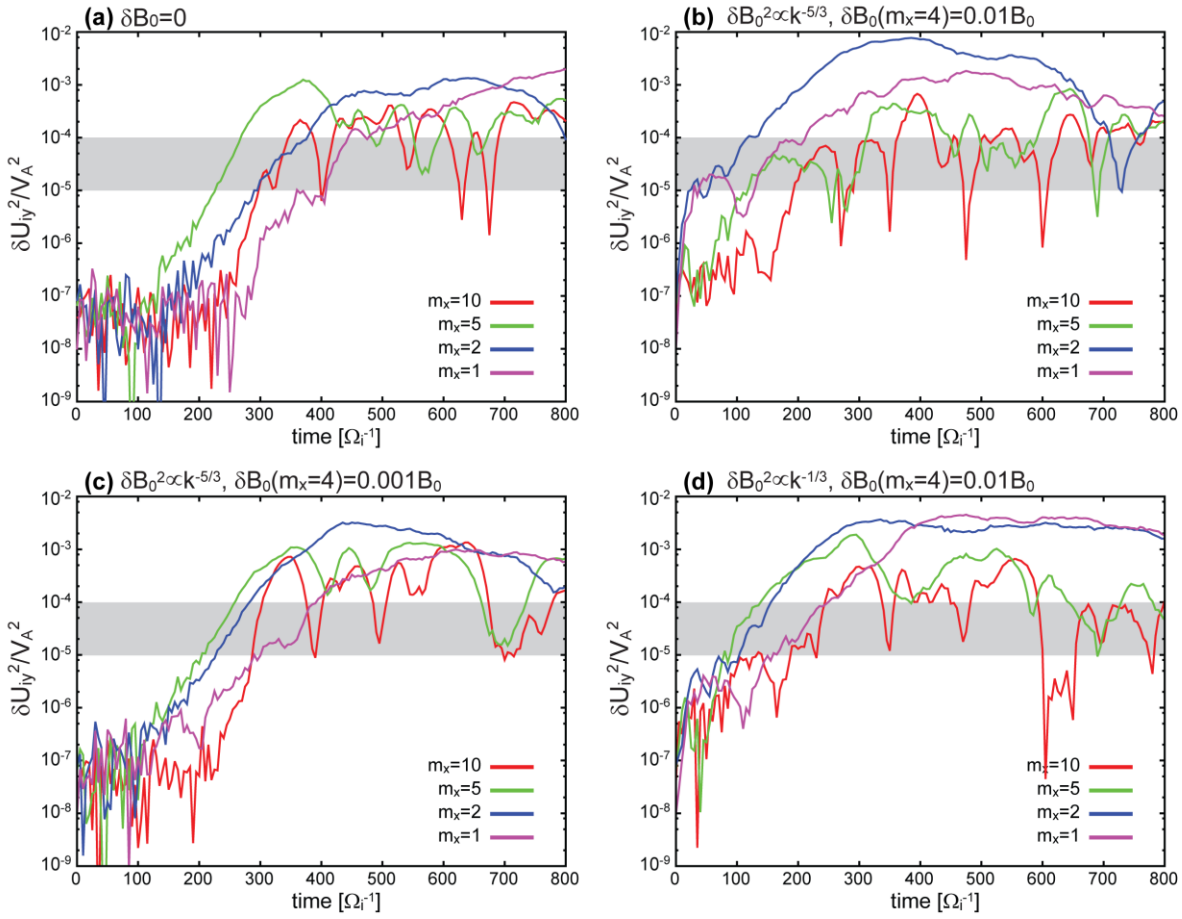

726

727 **Figure 6.** (a) Time evolution of U_{iy} modes at the center of the boundary (y=0) for m_x=10 (red), 5

728 (green), 2 (blue) and 1 (magenta) modes for runs-A (a), B (b), C (c) and E (d).

729

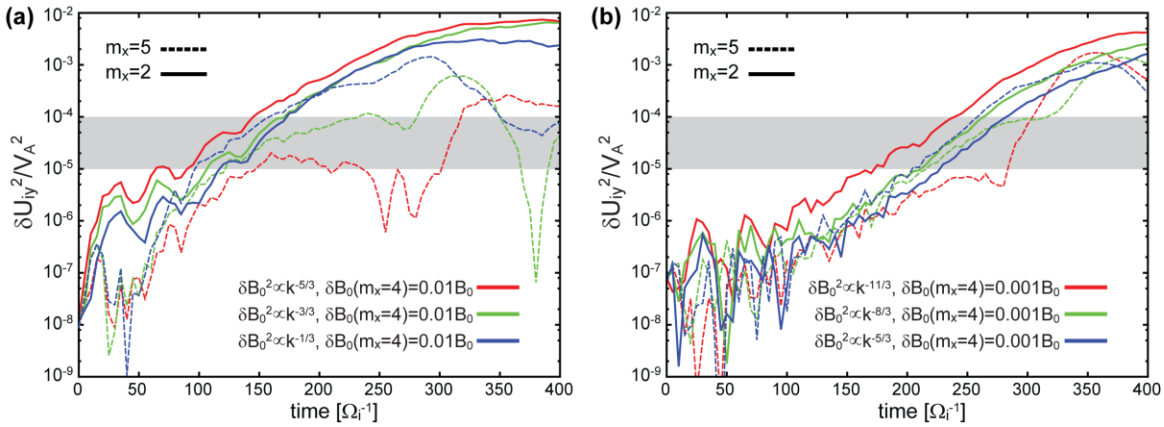

730

731 **Figure 7.** The same as Figure 6 but for m_x=5 (solid) and 2 (dashed) modes (a) with
732 $\delta B_0(m_x=4)=0.01B_0$ for runs-B ($\delta B_0^2 \propto k_x^{-5/3}$) (red), D ($\delta B_0^2 \propto k_x^{-1}$) (green), and E ($\delta B_0^2 \propto k_x^{-1/3}$)
733 (blue), and (b) with $\delta B_0(m_x=4)=0.01B_0$ for runs-F ($\delta B_0^2 \propto k_x^{-11/3}$) (red), G ($\delta B_0^2 \propto k_x^{-8/3}$) (green),
734 and C ($\delta B_0^2 \propto k_x^{-5/3}$) (blue).

735

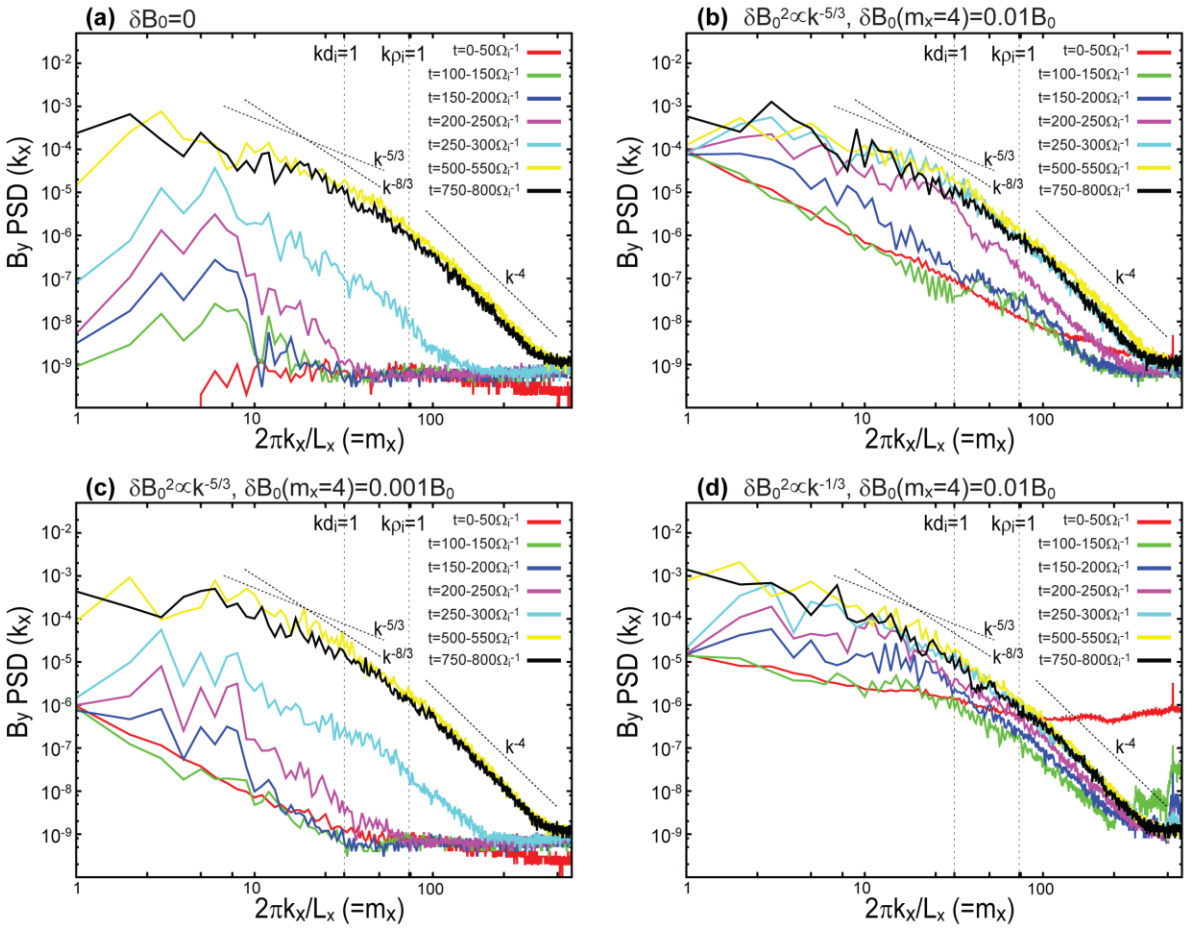

Figure 8. 1-D power spectra (k_x) of B_y averaged over t=0-50 Ω_i^{-1}, 100-150 Ω_i^{-1}, 150-200 Ω_i^{-1}, 200-250 Ω_i^{-1}, 250-300 Ω_i^{-1}, 500-550 Ω_i^{-1}, and 750-800 Ω_i^{-1}, around the center of the boundary (y=0±14.6 d_i) for runs-A (a), B (b), C (c) and E (d). The vertical lines indicate the wavelengths for $k_\perp \rho_i = 1$ and $k_\perp d_i = 1$.

741

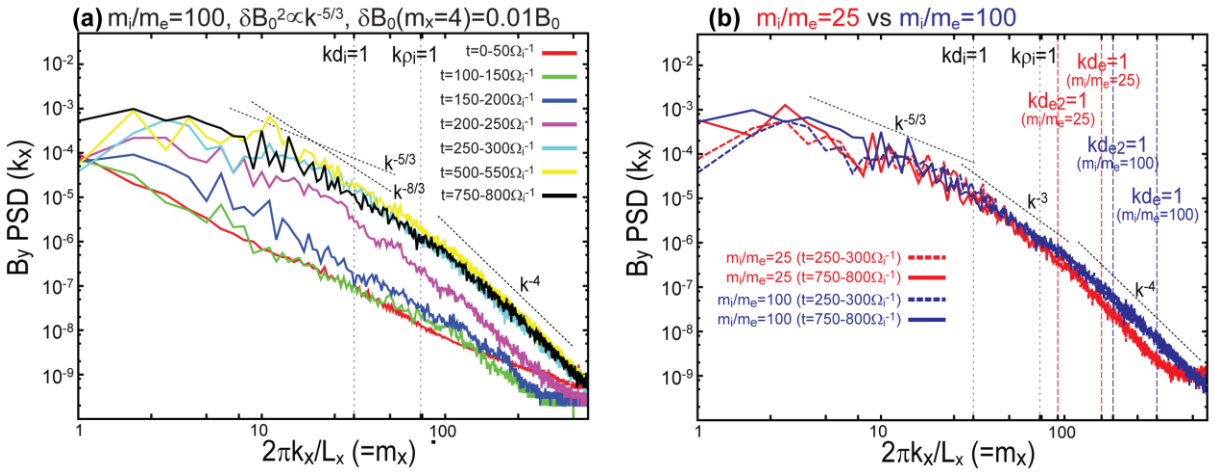

742

743 **Figure 9.** (a) The same as Figure 8b but for m_i/m_e=100. (b) Spectra of B_y averaged over t=250-
744 300 Ω_i^{-1} (dashed) and 750-800 Ω_i^{-1} (solid) for m_i/m_e=25 (red) and m_i/m_e=100 (blue). The vertical
745 colored lines indicate the wavelengths for $k_\perp d_e = 1$ and $k_\perp d_{e2} = 1$ for m_i/m_e=25 (red) and
746 m_i/m_e=100 (blue), where d_e and d_{e2} are the electron inertial lengths based on $n_1=n_0$ and n_2.

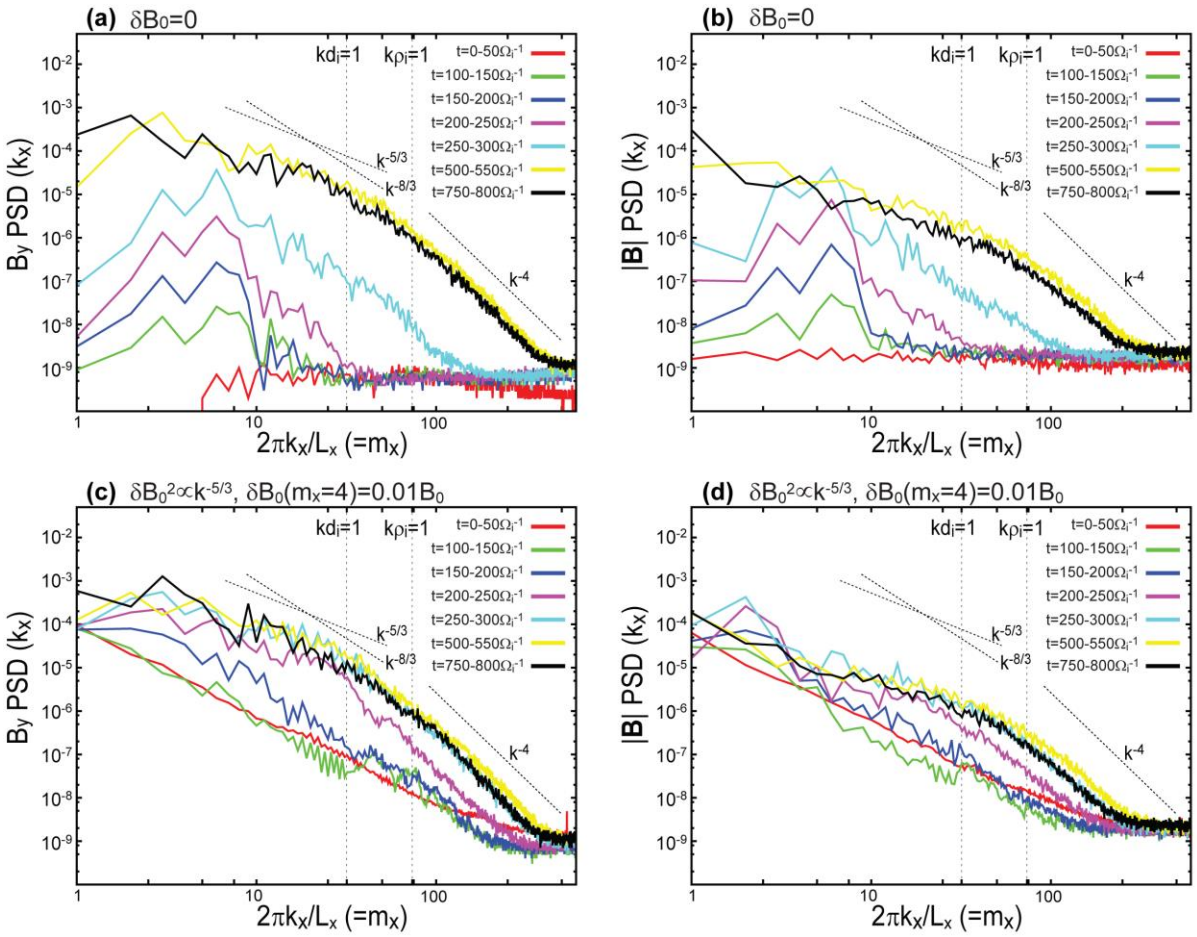

747

748 **Figure 10.** 1-D power spectra (k_x) for run-A (top) and run-B (bottom) of B_y (left) and |**B**| (right)
749 and B_y (bottom) for the same intervals and area as Figure 8. Figures 10a and 10c are the same as
750 Figures 8a and 8b.

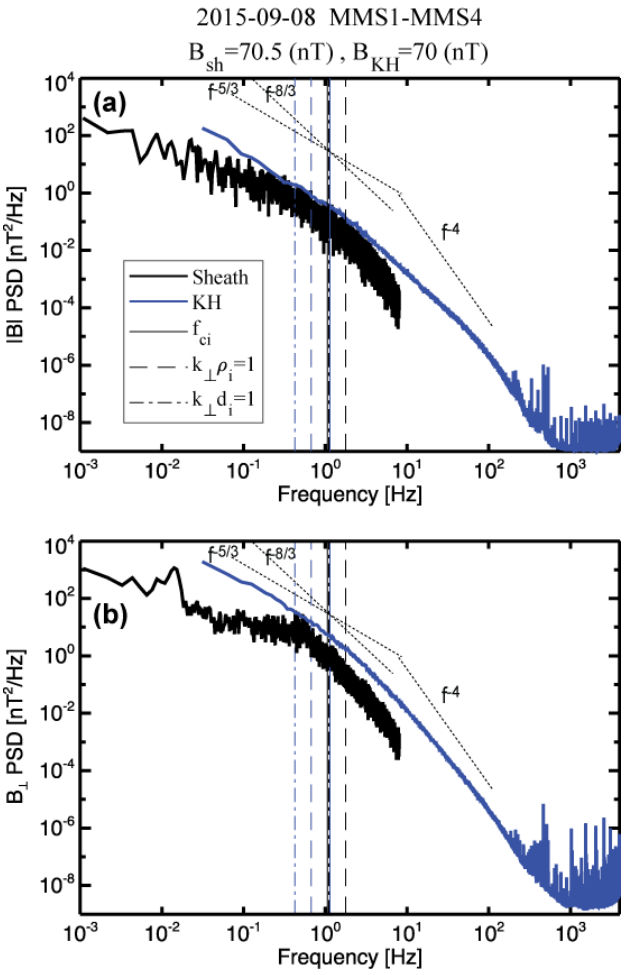

Figure 11. Averaged power spectra (Hz) of |**B**| (top) and the perpendicular component of the magnetic field $B_\perp$ (bottom) over the four MMS spacecraft and 38 selected intervals on 8 September 2015 during which MMS observed quasi-periodic KH waves for ~80 minutes at the postnoon (~16 MLT) magnetopause (see Stawarz et al. [2016] for more details about the techniques to obtain the averaged spectra of this event). The black curves show averaged spectra during the magnetosheath interval (11:35:00-11:50:20 UT). Here the magnetic field data during the KH interval are obtained from the Fluxgate Magnetometers (FGM) [Russell et al., 2016] and Search-Coil Magnetometer (SCM) [Le Contel et al., 2016], while the data during the magnetosheath interval are from the FGM. The vertical lines indicate the ion cyclotron frequencies f_{ci} and the wavelengths for $k_\perp \rho_i = 1$ and $k_\perp d_i = 1$ under the assumptions of Taylor hypothesis ($2\pi f = k_\perp V_\perp$).

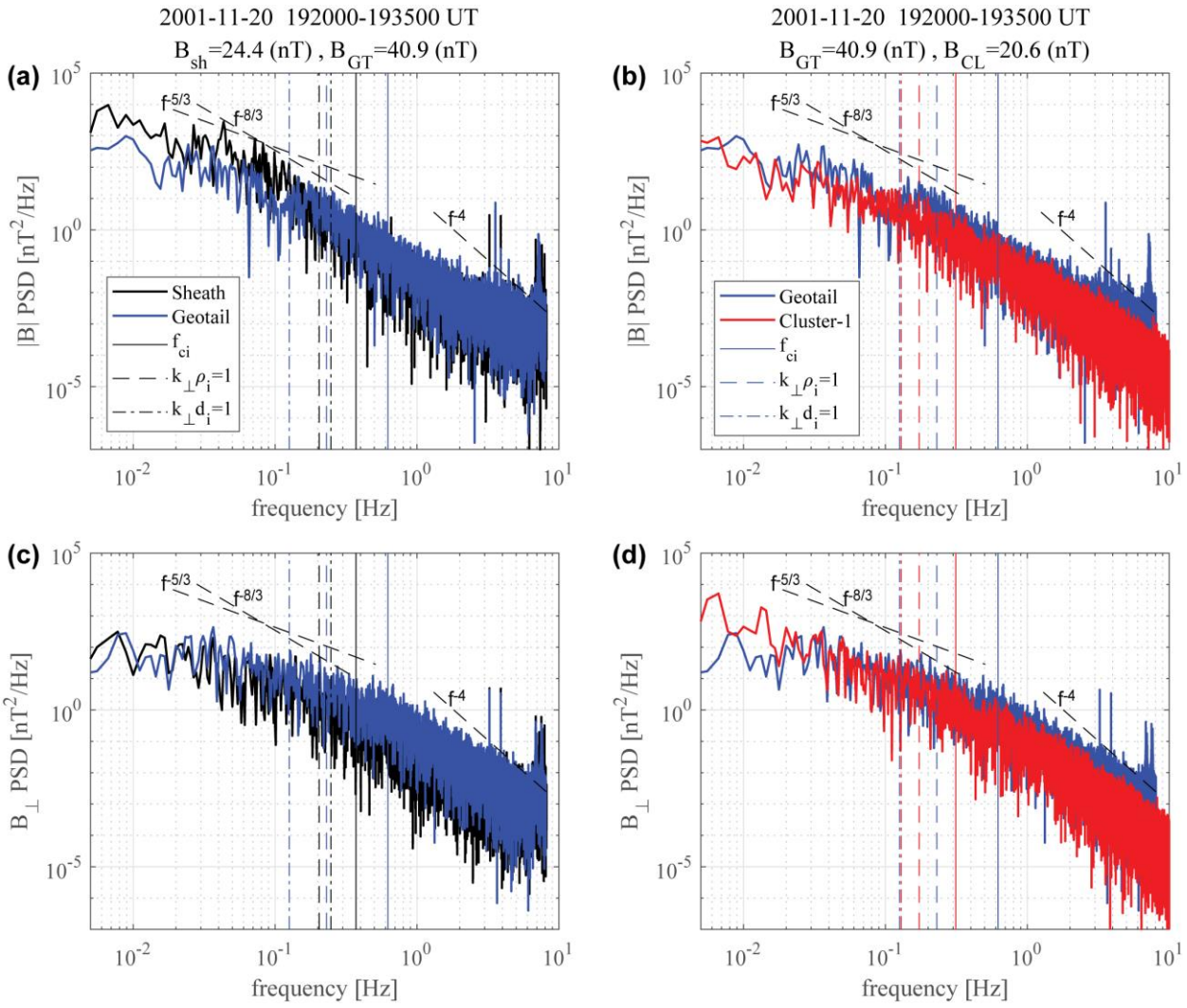

Figure 12. Averaged power spectra (Hz) of |**B**| (top) and $B_\perp$ (bottom) by Geotail (blue) and Cluster-1 (red) over 19:20-1935 UT on 20 November 2001, during which both Geotail and Cluster observed quasi-periodic KH waves at the postnoon (~15 MLT) and dusk-flank (~19 MLT) magnetopauses, respectively [Hasegawa et al., 2009]. The black curves show averaged spectra during the magnetosheath interval (19:00-1915 UT) observed by Geotail. Here the magnetic field data are obtained from the FGM for Cluster [Balogh et al., 2016] and the magnetic field experiment (MGF) for Geotail. The vertical lines indicate the ion cyclotron frequencies f_{ci} and the wavelengths for $k_\perp \rho_i = 1$ and $k_\perp d_i = 1$ under the assumptions of Taylor hypothesis ($2\pi f = k_\perp V_\perp$).

Figure 1.

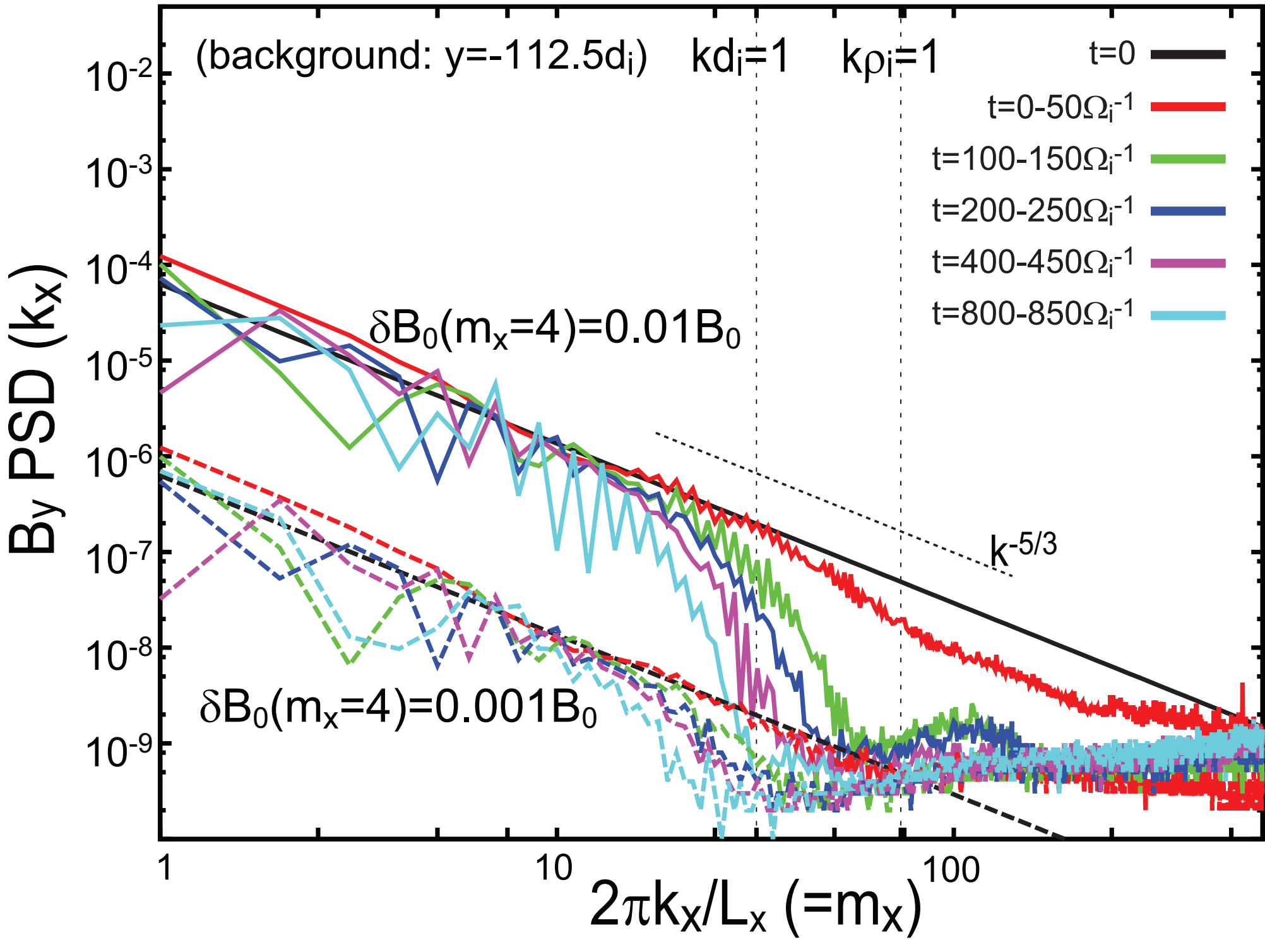
(background: y=-112.5d$_i$)
kd$_i$=1
kρ$_i$=1
t=0
t=0-50Ω$_i^{-1}$
t=100-150Ω$_i^{-1}$
t=200-250Ω$_i^{-1}$
t=400-450Ω$_i^{-1}$
t=800-850Ω$_i^{-1}$
δB$_0$(m$_x$=4)=0.01B$_0$
δB$_0$(m$_x$=4)=0.001B$_0$
k$^{-5/3}$
B$_y$ PSD (k$_x$)
2πk$_x$/L$_x$ (=m$_x$)
10^{-2}
10^{-3}
10^{-4}
10^{-5}
10^{-6}
10^{-7}
10^{-8}
10^{-9}
1
10
100

Figure 2.

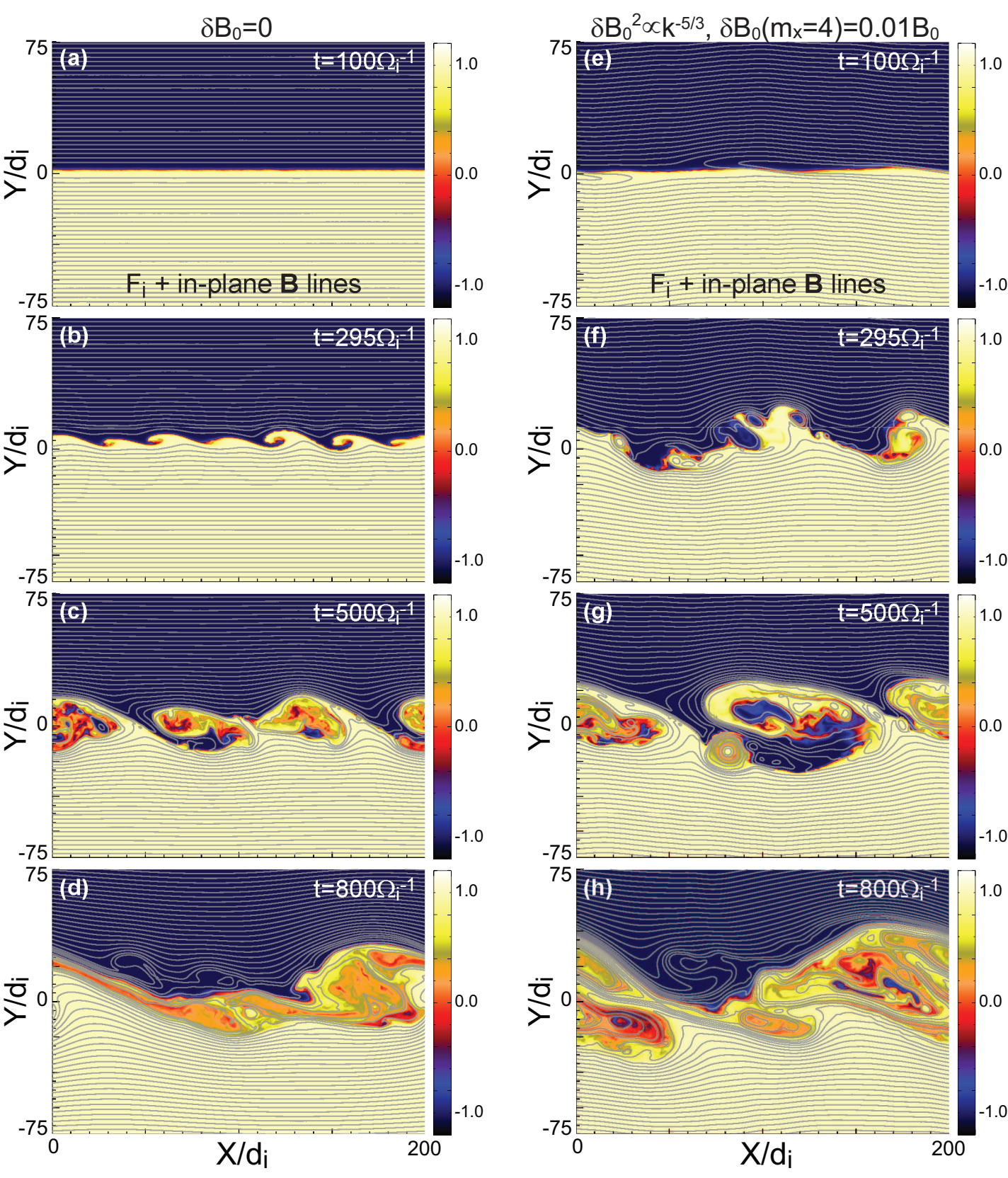
δB0=0
δB0²∝k^-5/3, δB0(mx=4)=0.01B0
(a)
t=100Ωi^-1
(b)
t=295Ωi^-1
(c)
t=500Ωi^-1
(d)
t=800Ωi^-1
(e)
t=100Ωi^-1
(f)
t=295Ωi^-1
(g)
t=500Ωi^-1
(h)
t=800Ωi^-1
Fi + in-plane B lines
Fi + in-plane B lines
Y/di
X/di
75
0
-75
200
1.0
0.0
-1.0

Figure 3.

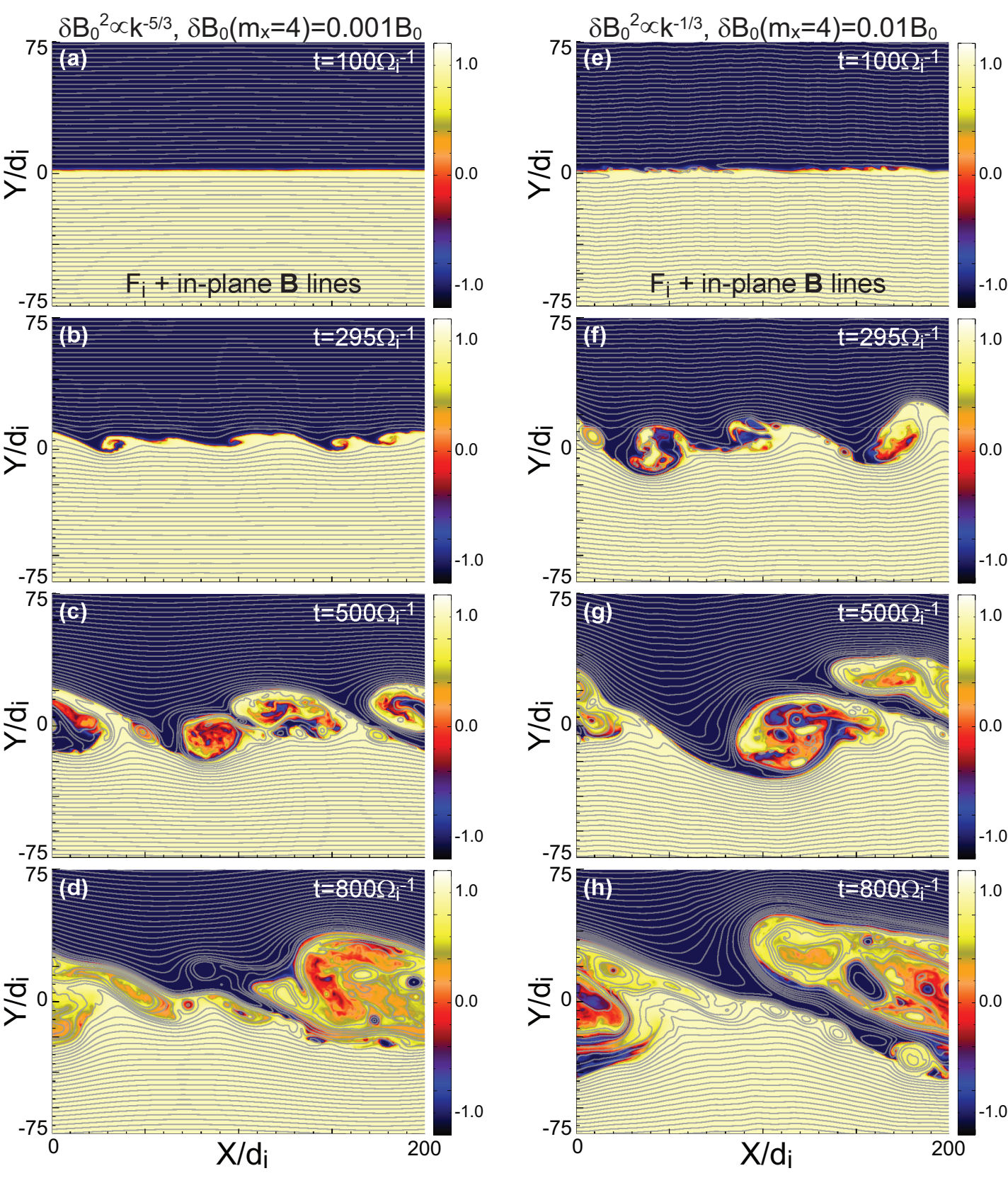
δB0^2∝k^-5/3, δB0(mx=4)=0.001B0
δB0^2∝k^-1/3, δB0(mx=4)=0.01B0
(a) t=100Ωi^-1
(b) t=295Ωi^-1
(c) t=500Ωi^-1
(d) t=800Ωi^-1
(e) t=100Ωi^-1
(f) t=295Ωi^-1
(g) t=500Ωi^-1
(h) t=800Ωi^-1
Fi + in-plane B lines
Y/di
X/di
75
0
-75
200
1.0
0.0
-1.0

Figure 4.

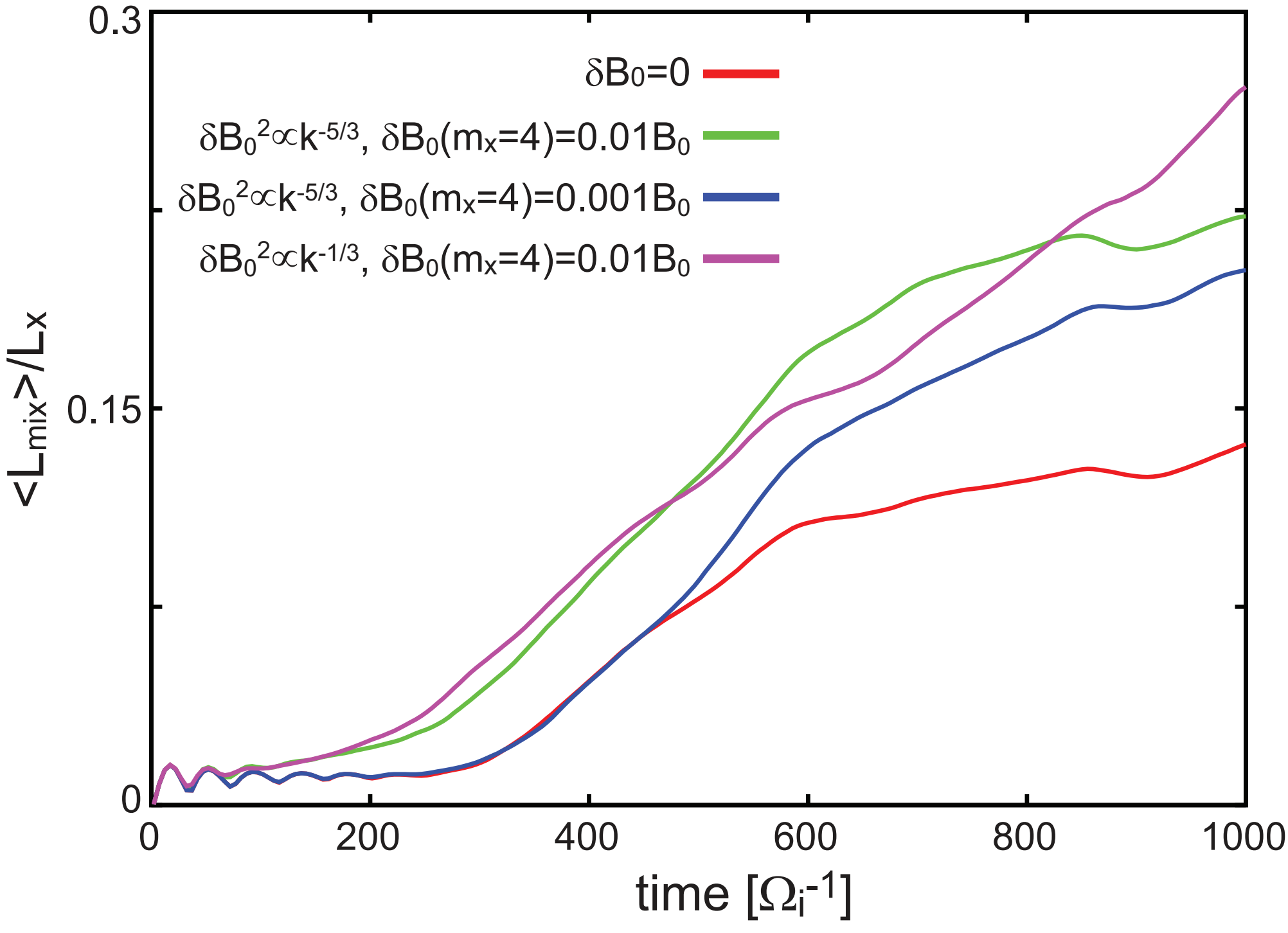
0.3
0.15
0
0
200
400
600
800
1000
<Lmix>/Lx
time [Ωi-1]
δB0=0
δB0²∝k-5/3, δB0(mx=4)=0.01B0
δB0²∝k-5/3, δB0(mx=4)=0.001B0
δB0²∝k-1/3, δB0(mx=4)=0.01B0

Figure 5.

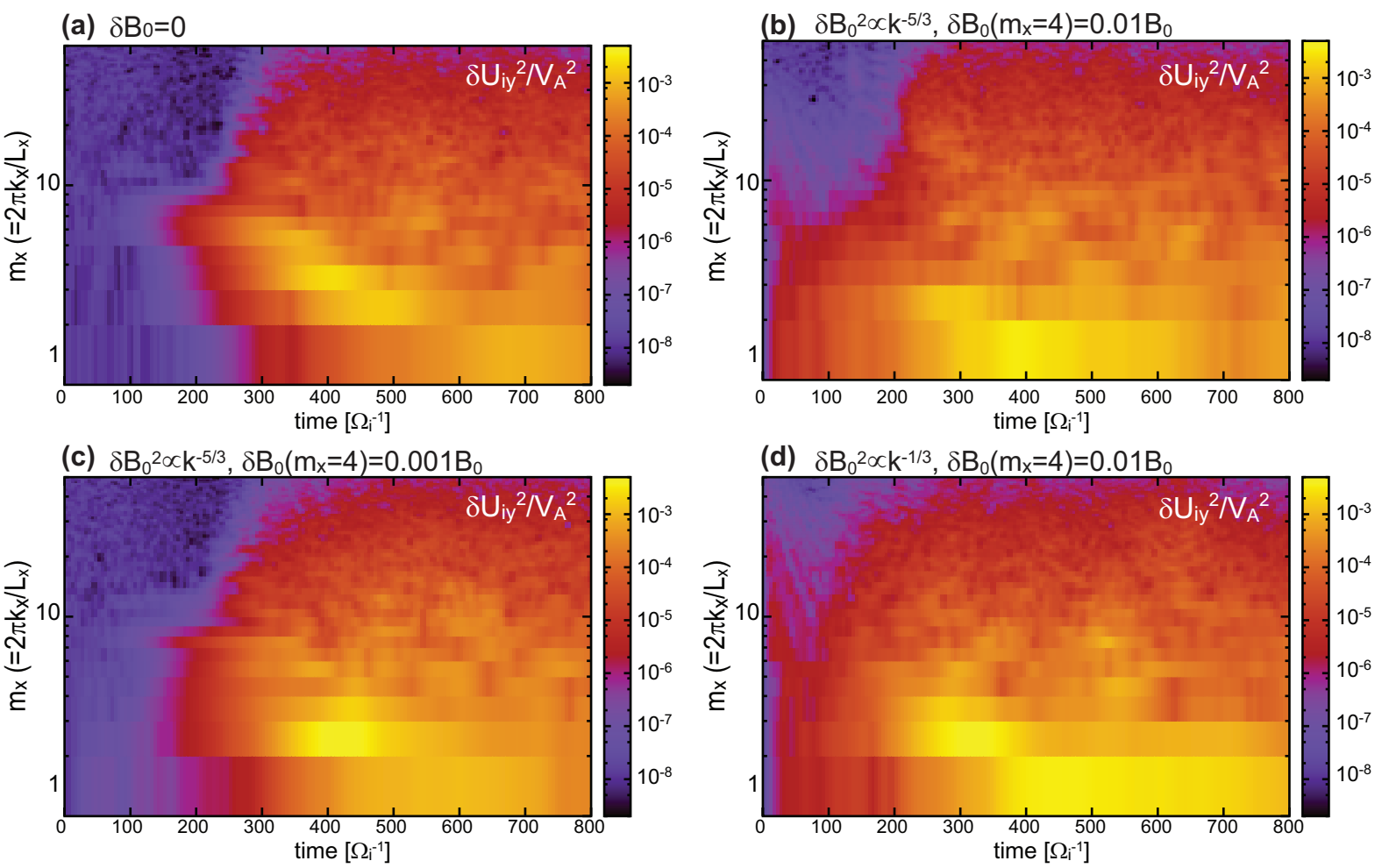
(a) δB0=0
(b) δB0²∝k^-5/3, δB0(mx=4)=0.01B0
(c) δB0²∝k^-5/3, δB0(mx=4)=0.001B0
(d) δB0²∝k^-1/3, δB0(mx=4)=0.01B0
δUiy²/VA²
mx (=2πkx/Lx)
time [Ωi^-1]
1
10
0
100
200
300
400
500
600
700
800
10^-3
10^-4
10^-5
10^-6
10^-7
10^-8

Figure 6.

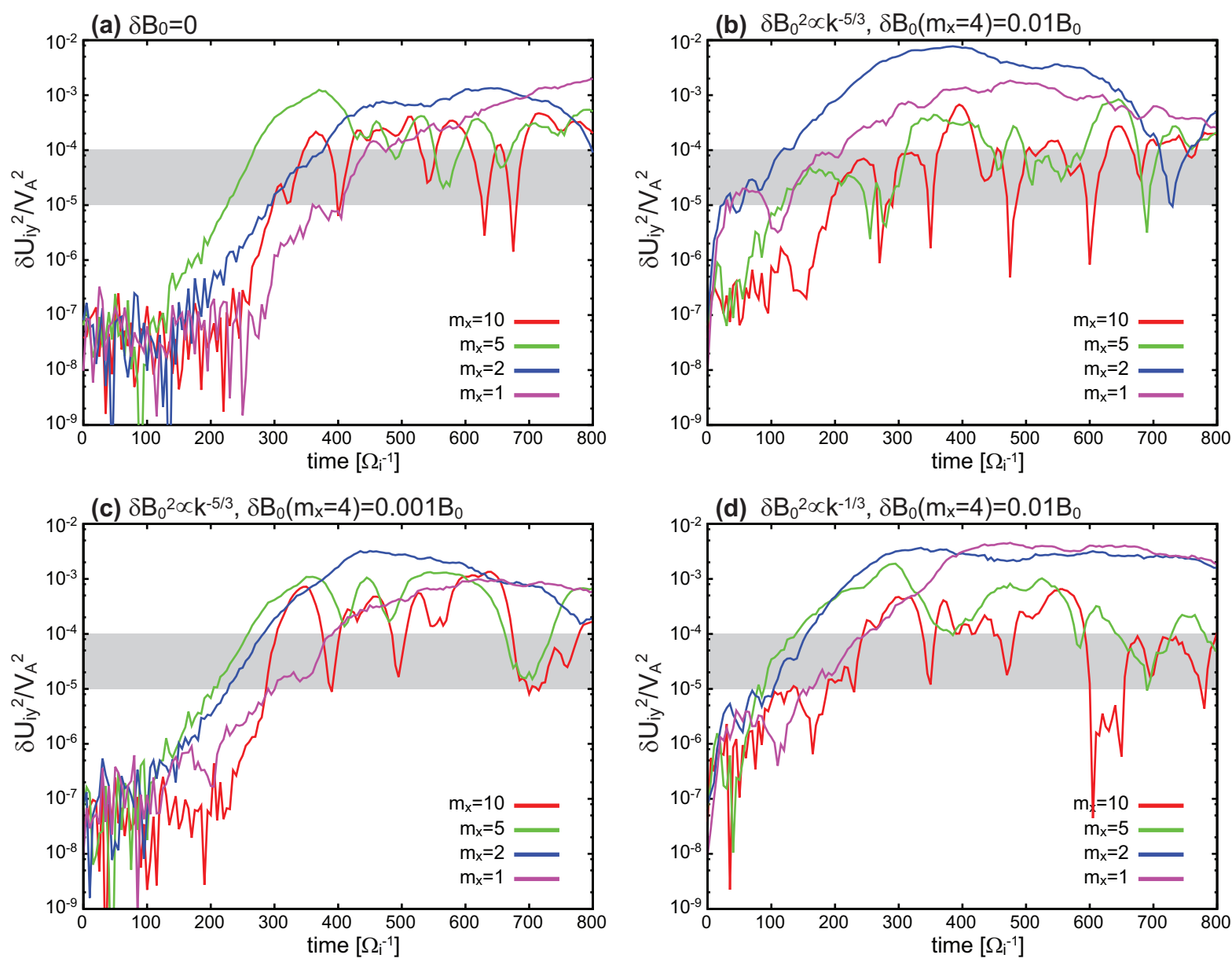
(a) δB0=0
(b) δB0²∝k^-5/3, δB0(mx=4)=0.01B0
(c) δB0²∝k^-5/3, δB0(mx=4)=0.001B0
(d) δB0²∝k^-1/3, δB0(mx=4)=0.01B0
δUiy²/VA²
time [Ωi^-1]
mx=10
mx=5
mx=2
mx=1

Figure 7.

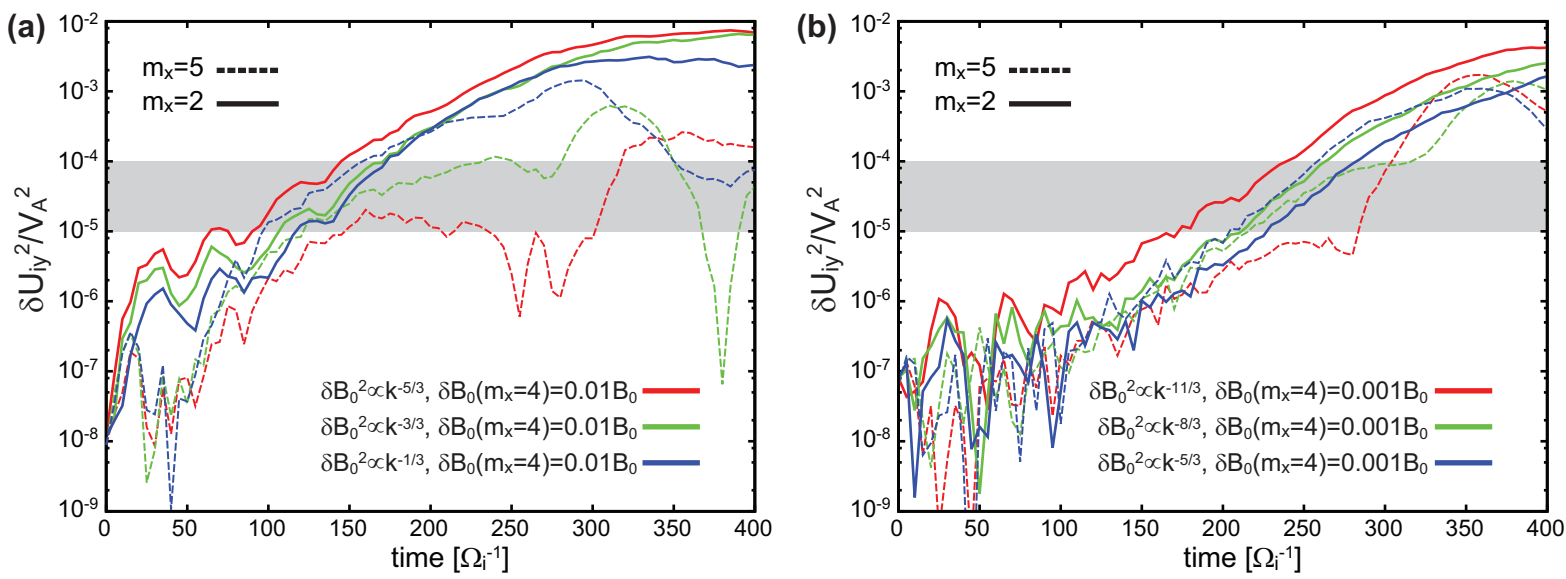
(a)
(b)
m_x=5
m_x=2
$\delta U_{iy}^2/V_A^2$
time [Ω_i^{-1}]
$\delta B_0^2 \propto k^{-5/3}$, $\delta B_0(m_x=4)=0.01B_0$
$\delta B_0^2 \propto k^{-3/3}$, $\delta B_0(m_x=4)=0.01B_0$
$\delta B_0^2 \propto k^{-1/3}$, $\delta B_0(m_x=4)=0.01B_0$
$\delta B_0^2 \propto k^{-11/3}$, $\delta B_0(m_x=4)=0.001B_0$
$\delta B_0^2 \propto k^{-8/3}$, $\delta B_0(m_x=4)=0.001B_0$
$\delta B_0^2 \propto k^{-5/3}$, $\delta B_0(m_x=4)=0.001B_0$

Figure 8.

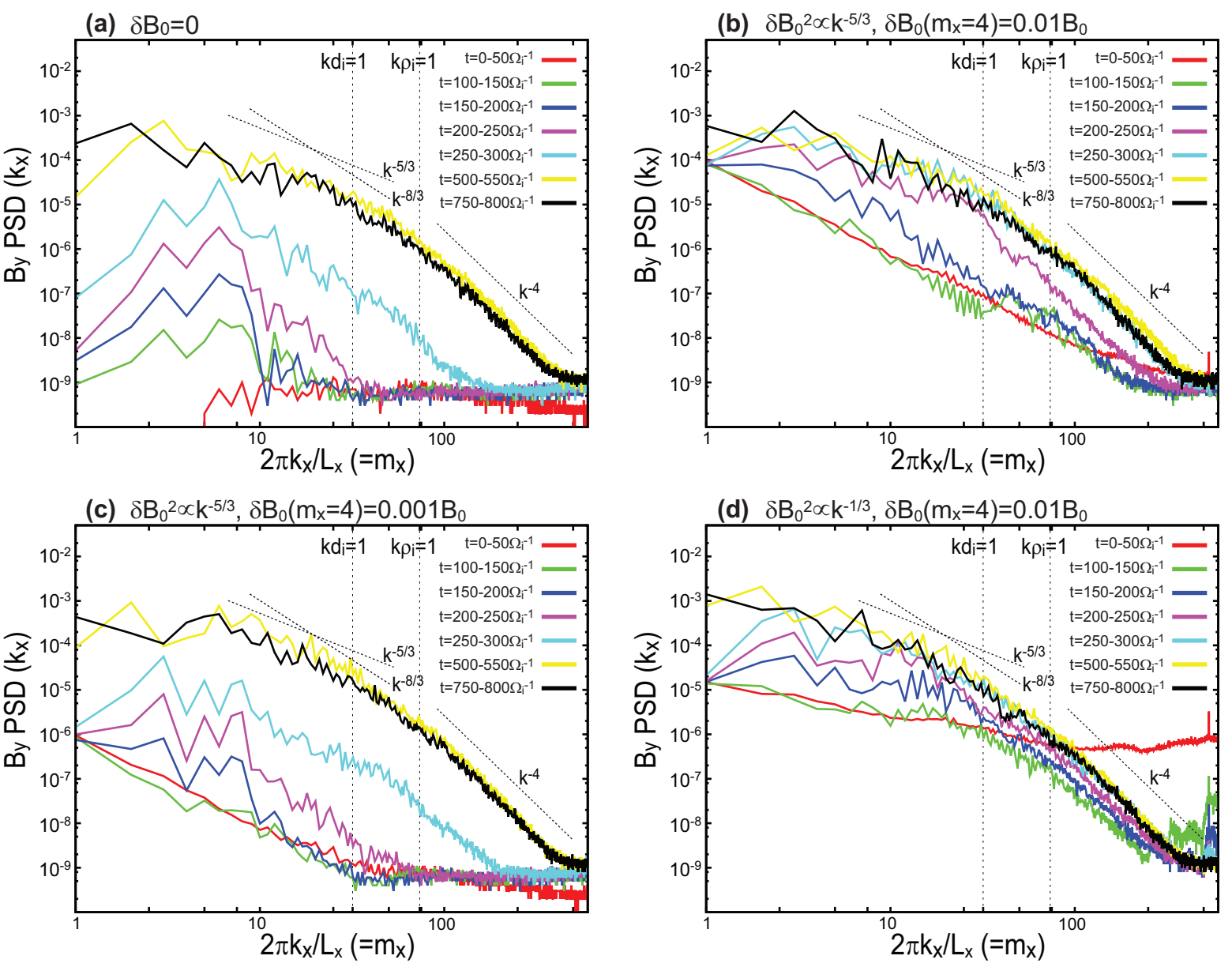
(a) δB0=0
(b) δB0²∝k^-5/3, δB0(mx=4)=0.01B0
(c) δB0²∝k^-5/3, δB0(mx=4)=0.001B0
(d) δB0²∝k^-1/3, δB0(mx=4)=0.01B0
kdi=1
kρi=1
t=0-50Ωi^-1
t=100-150Ωi^-1
t=150-200Ωi^-1
t=200-250Ωi^-1
t=250-300Ωi^-1
t=500-550Ωi^-1
t=750-800Ωi^-1
k^-5/3
k^-8/3
k^-4
By PSD (kx)
2πkx/Lx (=mx)

Figure 9.

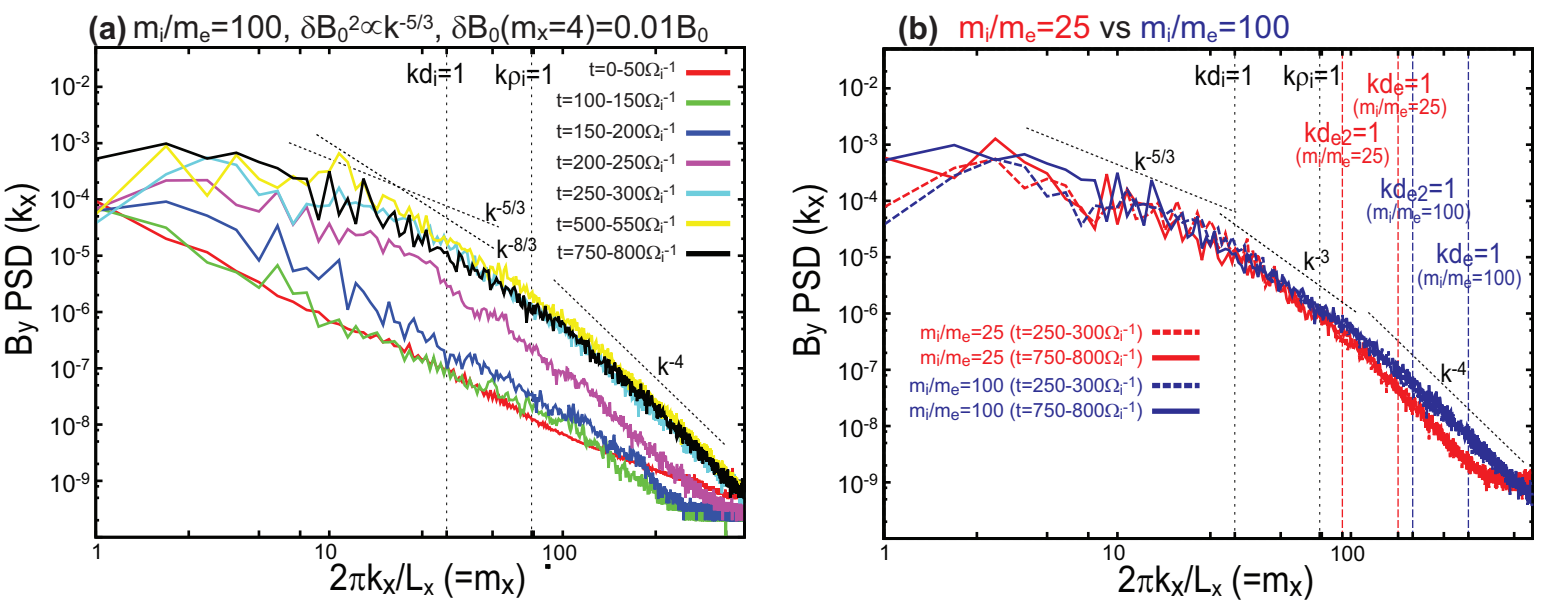
(a) m_i/m_e=100, $\delta B_0{}^2 \propto k^{-5/3}$, $\delta B_0(m_x$=4)=0.01B_0
kd_i=1
$k\rho_i$=1
t=0-50Ω_i^{-1}
t=100-150Ω_i^{-1}
t=150-200Ω_i^{-1}
t=200-250Ω_i^{-1}
t=250-300Ω_i^{-1}
t=500-550Ω_i^{-1}
t=750-800Ω_i^{-1}
$k^{-5/3}$
$k^{-8/3}$
k^{-4}
B_y PSD (k_x)
$2\pi k_x/L_x$ (=m_x)
(b) m_i/m_e=25 vs m_i/m_e=100
kd_i=1
$k\rho_i$=1
kd_e=1 (m_i/m_e=25)
kd_{e2}=1 (m_i/m_e=25)
kd_{e2}=1 (m_i/m_e=100)
kd_e=1 (m_i/m_e=100)
$k^{-5/3}$
k^{-3}
k^{-4}
m_i/m_e=25 (t=250-300Ω_i^{-1})
m_i/m_e=25 (t=750-800Ω_i^{-1})
m_i/m_e=100 (t=250-300Ω_i^{-1})
m_i/m_e=100 (t=750-800Ω_i^{-1})
B_y PSD (k_x)
$2\pi k_x/L_x$ (=m_x)

Figure 10.

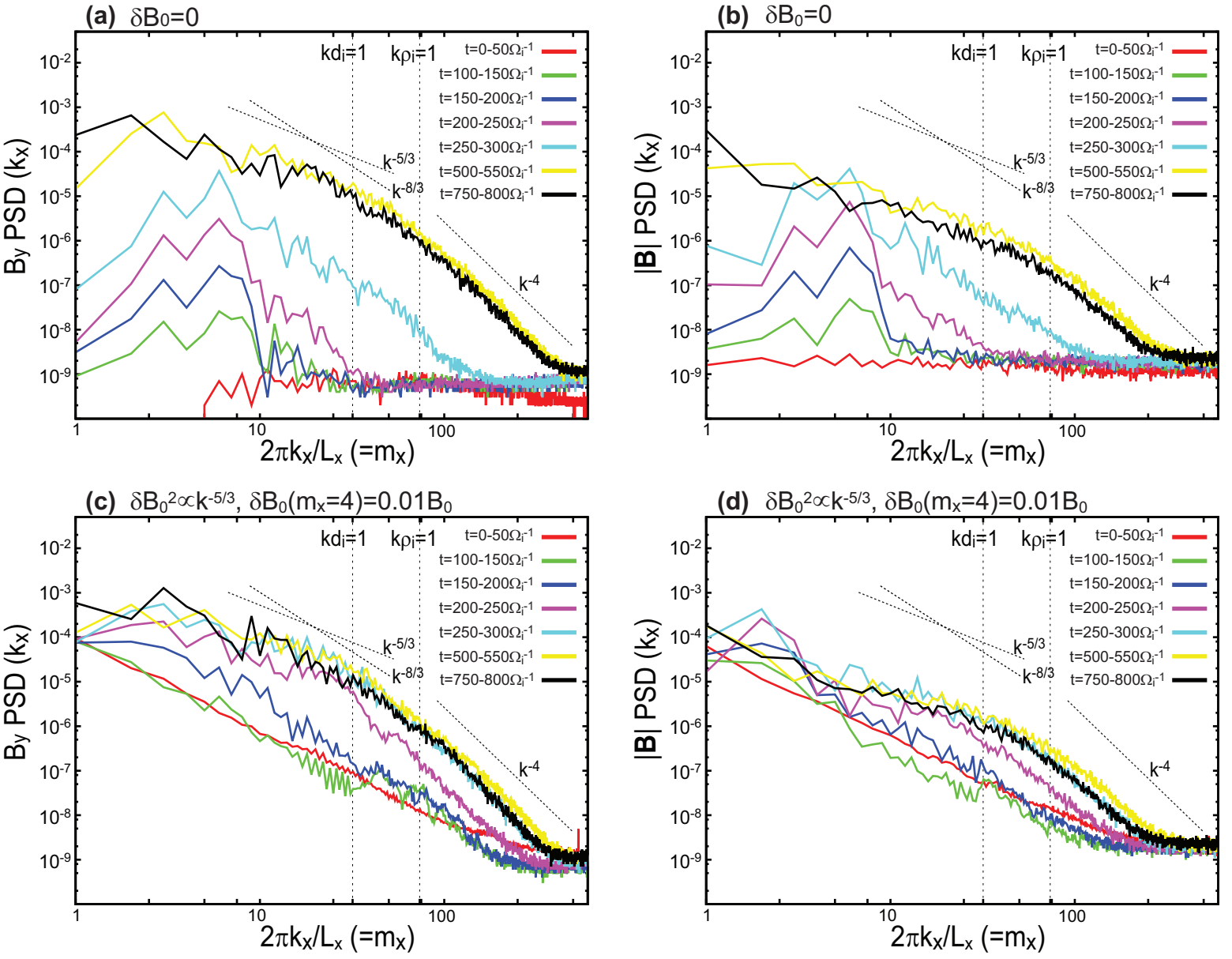
(a) δB0=0
(b) δB0=0
(c) δB0²∝k^-5/3, δB0(mx=4)=0.01B0
(d) δB0²∝k^-5/3, δB0(mx=4)=0.01B0
By PSD (kx)
|B| PSD (kx)
2πkx/Lx (=mx)
kdi=1
kρi=1
k^-5/3
k^-8/3
k^-4
t=0-50Ωi^-1
t=100-150Ωi^-1
t=150-200Ωi^-1
t=200-250Ωi^-1
t=250-300Ωi^-1
t=500-550Ωi^-1
t=750-800Ωi^-1

Figure 11.

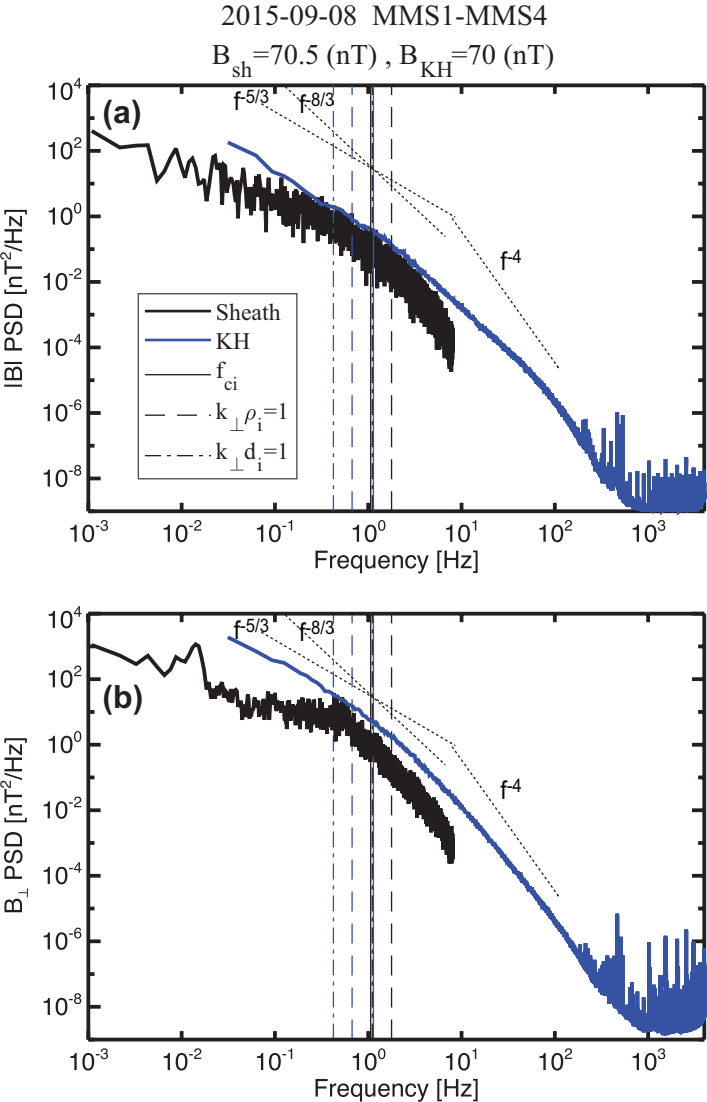
2015-09-08 MMS1-MMS4
B_sh=70.5 (nT) , B_KH=70 (nT)
(a)
f^-5/3
f^-8/3
f^-4
Sheath
KH
f_ci
k_⊥ρ_i=1
k_⊥d_i=1
|B| PSD [nT^2/Hz]
Frequency [Hz]
(b)
f^-5/3
f^-8/3
f^-4
B_⊥ PSD [nT^2/Hz]
Frequency [Hz]

Figure 12.

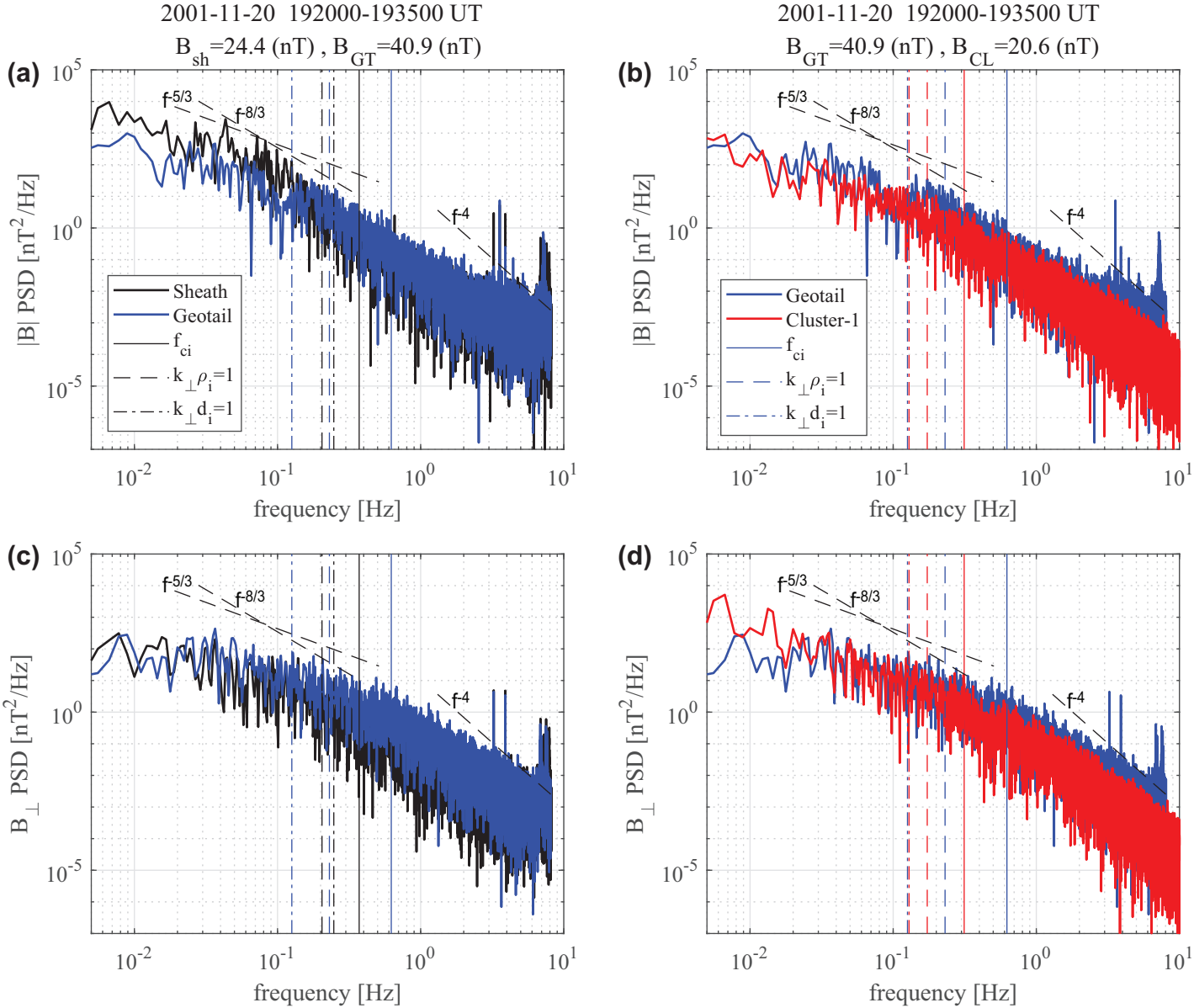
2001-11-20 192000-193500 UT
B_sh=24.4 (nT) , B_GT=40.9 (nT)
(a)
f^-5/3
f^-8/3
f^-4
Sheath
Geotail
f_ci
k_⊥ρ_i=1
k_⊥d_i=1
|B| PSD [nT^2/Hz]
frequency [Hz]
2001-11-20 192000-193500 UT
B_GT=40.9 (nT) , B_CL=20.6 (nT)
(b)
Geotail
Cluster-1
(c)
B_⊥ PSD [nT^2/Hz]
(d)